

Reduction and Protonation of Mo(IV) Imido Complexes with depe Coligands: Generation and Reactivity of a $S = 1/2$ Mo(III) Alkylidene Intermediate[†]

Ameli Dreher,^{‡,§} Sven Meyer,^{‡,§} Christian Näther,[‡] Anne Westphal,[‡] Henning Broda,[‡] Biprajit Sarkar,^{||,⊥} Wolfgang Kaim,[⊥] Philipp Kurz,^{*,‡,#} and Felix Tuczek^{*,‡}

[‡]Institut für Anorganische Chemie, Christian-Albrechts-Universität Kiel, Max-Eyth-Strasse 2, 24118 Kiel, Germany

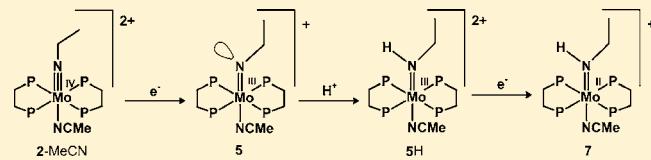
^{||}Institut für Chemie und Biochemie—Anorganische Chemie, Freie Universität Berlin, Fabeckstrasse 34 - 36 14195 Berlin, Germany

[⊥]Institut für Anorganische Chemie, Universität Stuttgart, Pfaffenwaldring 55, 70550 Stuttgart, Germany

[#]Institut für Anorganische und Analytische Chemie, Albert-Ludwigs-Universität Freiburg, Albertstrasse 21, 79104 Freiburg, Germany

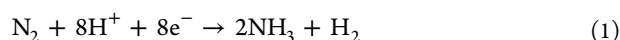
S Supporting Information

ABSTRACT: Reduction and protonation of Mo(IV) imido complexes with diphosphine coligands constitutes the second part of the Chatt cycle for biomimetic reduction of N_2 to ammonia. In order to obtain insights into the corresponding elementary reactions we synthesized the Mo(IV) ethylimido complex $[Mo(CH_3CN)(NEt)(depe)_2](OTf)_2$ (2-MeCN) from the Mo(IV)– NNH_2 precursor $[Mo(NNH_2)(OTf)(depe)_2](OTf)$ (1). As shown by UV–vis and NMR spectroscopy, exchange of the acetonitrile ligand with one of the counterions in THF results in formation of the so far unknown complex $[Mo(OTf)(NEt)(depe)_2](OTf)$ (2-OTf). 2-MeCN and 2-OTf are studied by spectroscopy and X-ray crystallography in conjunction with DFT calculations. Furthermore, both complexes are investigated by cyclic voltammetry and spectroelectrochemistry. The complex 2-OTf undergoes a two-electron reduction in THF associated with loss of the trans ligand triflate. In contrast, 2-MeCN in acetonitrile is reduced to an unprecedented Mo(III) alkylidene complex $[Mo(NEt)(CH_3CN)(depe)_2]OTf$ (5) which abstracts a proton from the parent Mo(IV) compound 2-MeCN, forming the Mo(III) ethylamido complex 5H and a Mo(II) azavinylidene complex 6. Compound 5 is also protonated to the Mo(III) ethylamido complex 5H in the presence of externally added acid and further reduced to the Mo(II) ethylamido complex 7. The results of this study provide further support to a central reaction paradigm of the Schrock and Chatt cycles: double reductions (and double protonations) lead to high-energy intermediates, and therefore, every single reduction has to be followed by a single protonation (and vice versa). Only in this way the biomimetic conversion of dinitrogen to ammonia proceeds on a minimum-energy pathway.



I. INTRODUCTION

Reduction of dinitrogen to ammonia by molecular catalysts continues to be one of the great challenges of bioinorganic and organometallic chemistry.¹ In the biosphere, the reaction is catalyzed by nitrogenase enzymes, the most active forms of which contain an iron–molybdenum cluster with (the FeMoco) as their catalytic site.^{2–5} Although mechanistic details of the reaction remain unclear, it can be stated that the $6e^-/6H^+$ reduction of dinitrogen (eq 1) probably occurs in a sequence of alternating $1e^-/1H^+$ reduction/protonation steps.^{2–5}



Transition-metal complexes containing dinitrogen ligands have served as model compounds to mimic key features of the nitrogenase reaction.^{6,7} One of the only two reported complete mechanistic schemes for biomimetic conversion of N_2 to NH_3 under ambient conditions is the Chatt cycle, which is based on

molybdenum and tungsten bis(dinitrogen) complexes that are supported by phosphine coligands.^{8,9}

Importantly, a number of intermediates for the Chatt cycle have been isolated and characterized, providing a detailed picture of transition-metal-centered conversion of dinitrogen to ammonia. The cycle starts with protonation of the metal-bound N_2 , consecutively leading to $M(IV)–NNH$, $M(IV)–NNH_2$, and $M(IV)–NNH_3$ complexes ($M = Mo, W$).^{6,8,10,11} Cleavage of the $N–N$ bond is achieved by the two-electron reduction of $M(IV)–NNH_2$ complexes. Detailed information concerning this process has been obtained from studies of dialkylhydrazido(2–) complexes $[M(NNR_2)(dppe)_2Br]Br$ ($dppe = 1,2$ -bis(diphenylphosphino)ethane) which, after two-electron reduction and halide loss, form neutral, five-coordinate $M(II)$ complexes $[M(NNR_2)(dppe)_2]$.^{6,12} If acid is added to such

Received: August 21, 2012

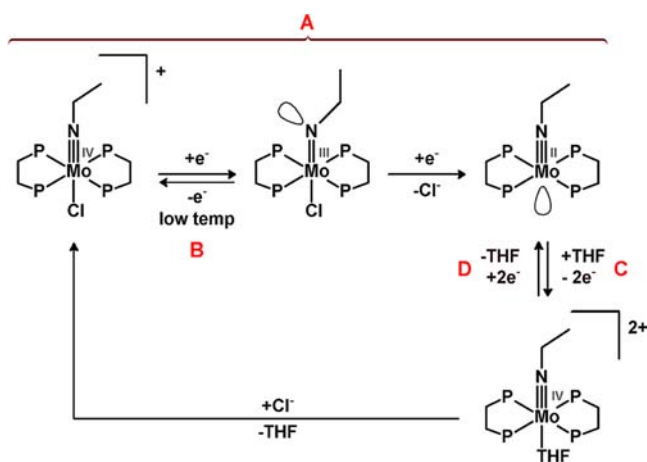
Published: February 11, 2013



compounds, the N–N bond is cleaved, generating a first equivalent of ammonia and M(IV) nitrido or imido species.

In the second half of the Chatt cycle the Mo(IV) or W(IV) nitrido or imido complexes are converted back to the M(0) bis(dinitrogen) starting compounds. This process involves four reduction and three protonation steps, yielding a second molecule of ammonia. To reveal details of these reaction steps, alkylimido complexes are preferentially studied because undesired intermolecular acid–base reactions and H₂ evolution complicate investigation of the nonalkylated complexes. In 1997, Alias et al. followed this strategy and studied the redox properties of the Mo(IV) alkylimido compounds [MoX(NEt)(dppe)₂]⁺ (2-dppe-X, X = Hal) by cyclic voltammetry (CV) and coulometric analysis.¹³ The measurements demonstrated that these ethylimido complexes could be irreversibly reduced at rather low potentials (−2.2 V for X = Cl; −2.0 V for X = I). Reoxidation of the reduction product occurred at an identical potential (−1.6 V) for both 2-dppe-Cl and 2-dppe-I, which the authors took as evidence that, upon reduction of the starting Mo(IV) compounds, the axial halogenido ligand is lost, resulting in formation of the same five-coordinate [Mo(NEt)(dppe)₂] species for both the chlorido and the iodido system. Coulometric analysis of the reduction event showed that a two-electron process occurs, i.e., the five-coordinate reduction product obtained at ~−2 V should be a Mo(II) complex. With respect to the reaction mechanism, it was assumed that the axial halogenido ligand is cleaved off after transfer of the first electron to generate a five-coordinate Mo(III) intermediate with a higher reduction potential than the parent compound so that a second electron is transferred immediately (Scheme 1A).

Scheme 1. Reactions Reported for [MoCl(NEt)(dppe)₂]⁺ (2-dppe-Cl) Following the Electrochemical Reduction of the Complex at −2.2 V^a



^aProcess A modified from Alias et al.¹³

This hypothesis was supported by the fact that reductions of 2-dppe-Cl and 2-dppe-I became partly reversible at low temperatures ($T = -36\text{ }^{\circ}\text{C}$), which should slow down the loss of the trans ligand (Scheme 1B).

Reoxidation at −1.6 V was assumed to occur as a two-electron process as well, this time accompanied by coordination of a solvent molecule (Scheme 1C). In a second scan, a new reduction peak was observed at −1.75 V, which was attributed to the reduction of the solvent-coordinated Mo(IV) ethylimido complex (Scheme 1D).

When Alias et al. carried out electrochemical reductions in the presence of phenol as a proton source, the reoxidation peak of the five-coordinate species disappeared in favor of a new peak at less negative potentials. This was demonstrated for the related complex [MoX(NCH₂Ph)(dppe)₂]⁺ (X = Hal).¹³ If rapid scans are performed in the CV experiment, this species also shows reversible reduction behavior. More importantly, the potential of the oxidation in this case *does* depend on the type of trans ligand, as shown for different halide ligands.¹³ The results indicated that for [MoX(NCH₂Ph)(dppe)₂]⁺ the reduction event is followed by protonation of the coordinated benzylimido ligand while the trans ligand X[−] is retained.¹³ Thus, it could be concluded that in this case a one-electron reduction event is followed first by protonation of the nitrogen ligand and only then by a second reduction.¹³

In the detailed investigation presented here, we report electrochemical reduction reactions for the cationic ethylimido complexes [Mo^{IV}(L)(NEt)(depe)₂]^{2+/+} (2-L; L = MeCN or OTf; MeCN = acetonitrile, OTf = triflate, depe = 1,2-bis(diphenylphosphino)ethane), compounds that are closely related to the systems studied by Alias et al. As it was our aim to complement electrochemical measurements in different solvents with UV–vis spectroelectrochemistry, the dppe ligands of the former complexes were replaced by aliphatic depe ligands. This allowed us to detect absorption bands in the ligand-field (LF) region, providing information about the electronic structures of reaction intermediates. In the case of dppe compounds, these electronic transitions would be masked by the intense transitions of the aromatic phenylphosphine groups.^{10,14}

Complex 2-MeCN was synthesized starting from the Mo(IV)–NNH₂ precursor [Mo(NNH₂)(OTf)(depe)₂](OTf) (1) by a new route (see below). The weakly coordinating triflate anion functions as counterion to the cationic complex 2-MeCN. When 2-MeCN is dissolved in acetonitrile, the initial coordination sphere is preserved. In tetrahydrofuran (THF), on the other hand, the acetonitrile ligand is replaced by a triflate anion, resulting in formation of [Mo^{IV}(OTf)(NEt)(depe)₂]⁺ (2-OTf; for details, see below). In order to obtain a firm basis for the intended studies, the molecular structures, spectroscopic properties, and ligand-exchange phenomena for 1, 2-MeCN, and 2-OTf are analyzed in detail, as will be presented in the first sections of the Results and Analysis. Then cyclic voltammetric and spectroelectrochemical data collected for electrochemical reductions of both 2-MeCN and 2-OTf in the presence and absence of phenol will be considered. Whereas reduction of 2-OTf follows the two-electron pathway established earlier, reduction of 2-MeCN in acetonitrile leads to a one-electron-reduced species, an $S = 1/2$ Mo(III) alkylnitrene complex (5), which is protonated to the Mo(III) alkylamido complex 5H and further reduced to the Mo(II) alkylamido complex 7. The implications of these results with respect to the Chatt cycle and the biomimetic reduction of N₂ to ammonia are discussed.

II. EXPERIMENTAL SECTION

A. Sample Preparation. All reactions and sample preparations were performed under nitrogen or argon atmospheres using Schlenk techniques. All solvents were dried under argon. Sample manipulations for all spectroscopic investigations were carried out in a glovebox.

Syntheses of [Mo(OTf)(NNH₂)(depe)₂](OTf) (1-OTf) and [Mo(MeCN)(NEt)(depe)₂](OTf) (2-MeCN) were carried out as described earlier.¹⁵

1. Synthesis of [Mo(OTf)(NEt)(depe)₂](OTf) (2-OTf). To 500 mg of [Mo(MeCN)(NEt)(depe)₂](OTf)₂ (2-MeCN) 20 mL of THF was

added, and the resulting suspension was stirred overnight. On the next day, the solvent of the resulting pink solution was removed in vacuo and the residue was dissolved in THF again. The complex was precipitated by addition of diethyl ether, filtered off, washed with diethyl ether, and dried in vacuo. A pink solid was obtained in nearly quantitative yield. Anal. Calcd: N, 1.52; C, 36.49; H, 6.67; S, 6.96. Found: N, 1.59; C, 36.10; H, 6.69; S, 7.00. For ^{19}F NMR and UV–vis spectroscopy, see below. IR and further NMR spectroscopic data can be found in the Supporting Information (Figures S1–S3).

B. X-ray Crystallography. Intensity data of 2-OTf·THF were collected using a STOE imaging plate diffraction system (IPDS-1) with Mo K α radiation (Table 1). The structure was solved with direct

Table 1. Crystal Data and Structure Refinement for 2-OTf

	2-OTf
formula	$\text{C}_{28}\text{H}_{61}\text{F}_6\text{MoNO}_7\text{P}_4\text{S}_2$
MW/g·mol $^{-1}$	921.72
cryst color	pink
cryst syst	monoclinic
space group	$P2_1$
<i>a</i> , Å	10.5000 (6)
<i>b</i> , Å	15.7795 (12)
<i>c</i> , Å	12.9565 (7)
β , deg	103.844 (6)
<i>V</i> , Å 3	2084.3 (2)
temp., K	170 (2)
<i>Z</i>	2
<i>D</i> _{calcd.} , g·cm $^{-3}$	1.469
<i>F</i> (000)	960
2 θ range	4.8–54.2°
<i>h</i> / <i>k</i> / <i>l</i> ranges	–12/12, –20/20, –16/16
μ , mm $^{-1}$	0.635
no. of measd reflns	20 909
<i>R</i> _{int.}	0.0317
no. of independent reflns	8907
no. of reflns with <i>I</i> > 2 σ (<i>I</i>)	8326
no. of refined params	451
<i>R</i> ₁ [<i>I</i> > 2 σ (<i>I</i>)]	0.0374
wR_2 [all data]	0.0934
GoF	1.085
min/max residuals, e·Å $^{-3}$	1.218/–0.685
Flack <i>x</i> parameter	–0.01(3)

methods using SHELXS-97, and refinement was performed against *F* 2 using SHELXL-97.¹⁶ All non-hydrogen atoms with the exception of two disordered O atoms of the THF molecule were refined anisotropically. C–H hydrogen atoms were positioned with idealized geometries and refined using a riding model. Two carbon atoms of the THF molecule were found to be disordered and thus refined using a split model. The absolute structure was determined and is in agreement with the selected setting (Flack *x* parameter 0.01(3)). CCDC 923453 contains the supplementary crystallographic data for this paper, which can be obtained free of charge from the Cambridge Crystallographic Data Center via www.ccdc.cam.uk/data_request.cif.

C. NMR Spectroscopy. NMR spectra were recorded on a Bruker Avance 400 pulse Fourier transform spectrometer operating at a ^1H frequency of 400.13 MHz (^{31}P 161.98 MHz, ^{19}F 376.50 MHz) and equipped with a 5 mm inverse triple-resonance probe head. References as substitutive standards: H_3PO_4 85% pure, δ (^{31}P) = 0 ppm, and $\text{CFCl}_3/\text{CDCl}_3$, δ (^{19}F) = 0 ppm, were used.

D. UV–Vis Spectroscopy. UV–vis spectra were recorded in solution or KBr pellets with a Cary 5000 UV–vis–NIR spectrometer (Varian) from 190 to 1020 nm with a resolution of <0.05 nm.

E. DFT and TDDFT Calculations. All calculations were performed using Becke's three-parameter hybrid functional with the LYP correlation functional of Lee, Yang, and Parr.¹⁷ The LANL2DZ basis

set was used for the Mo metal center, while the 6-31G* set described nonmetal atoms.¹⁸ For calculation of MO schemes and optical transitions of 2-MeCN and 2-OTf, 5, 5H, 6, and 7, the diphosphine ligands (depe) were simplified to $\text{H}_2\text{PCH}_2\text{CH}_2\text{PH}_2$ (the truncated complexes are abbreviated as 2-OTf, 2-MeCN, 5, 5H, 6, and 7). All computational procedures were carried out as implemented in the Gaussian-09 software package.¹⁹ Wave functions were plotted using Gaussview 5.0.

F. Electrochemistry. Electrochemical measurements were performed with an EG&G PAR M273A potentiostat controlled by the PowerSuite software package. For cyclic voltammetry measurements, a platinum disc working electrode (Metrohm, disc diameter 1 mm), a platinum counter electrode, and a Ag/Ag $^+$ reference electrode (silver wire immersed in 0.01 M AgNO_3 in THF (2-OTf) or MeCN (2-MeCN), –87 mV vs Fc/Fc $^+$) were used. Measurements were performed at room temperature in 1 mM (15 mM for UV–vis spectroelectrochemistry) solutions of the compounds in THF (2-OTf) or MeCN (2-MeCN) containing 0.1 M tetrabutylammonium hexafluorophosphate (NBu_4PF_6) as conducting electrolyte. Coulometric measurements were performed in an identical setup with the only difference of using a platinum net (ca. 14 cm 2) as working electrode. UV–vis spectroelectrochemical measurements were performed in an optically transparent thin layer electrochemical (OTTLE) cell (layer thickness 1.0 mm; see Supporting Information, Figure S4) with a platinum net working electrode, a platinum counter electrode, and a Ag/Ag $^+$ reference electrode (vide supra). In each case, measurements were performed in carefully dried, degassed solutions under an argon atmosphere. All redox potentials in this paper are given versus the potential of the ferrocene–ferrocenium couple in the respective solvents. For convenient comparison with the important reference data on related systems obtained by Alias et al., all cyclic voltammograms were plotted using the same current and voltage convention as in ref 13.

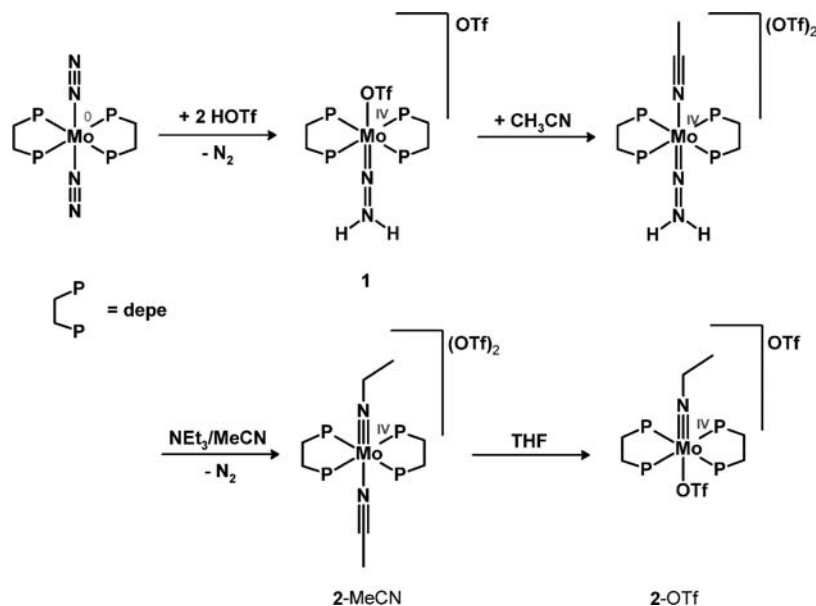
G. EPR Spectroscopy. Room-temperature cw X-band EPR spectroelectrochemistry measurements were performed using a Bruker EMXplus spectrometer with a PremiumX microwave bridge and a HQ X-band cavity controlled by a computer running the Bruker Xenon 1.0 software. EPR spectra were recorded after electrolysis of the solution sample in a 4 mm quartz EPR tube containing a two-electrode setup of platinum working and counter electrodes (see Supporting Information, Figure S5).²⁰ Sample solutions of 2-MeCN in acetonitrile (10 mM) were prepared under a protective argon atmosphere. Again, NBu_4PF_6 (0.1 M) was used as electrolyte. As no reference electrode could be used due to space restrictions in the EPR tube, at the start reduction potentials of the working electrode were slowly increased using a conventional dc power supply unit until a current of 30–40 μA between the two electrodes was established. Samples were then electrolyzed for several minutes at this constant potential to obtain samples of sufficient EPR signal intensities. EPR spectra were simulated using MATLAB (MathWorks Inc.) employing the “garlic” simulation function for fast-motion cw EPR spectra of the EasySpin toolbox (v. 4.0.0).²¹ Only simulations with isotropic parameters are shown, as simulations employing an anisotropic model yielded virtually identical results (Supporting Information, Figures S6 and S7).

III. RESULTS AND ANALYSIS

A. Synthesis and Spectroscopic Characterization of 1 and 2. Alkylimido complexes are usually prepared by alkylation of nitrido complexes.^{22,23} As reported earlier by us, a special route can be used if ethylimido complexes are to be synthesized (Scheme 2).¹⁵ Here, acetonitrile serves as a source for the ethylimido ligand, thus avoiding formation of mixed counterions associated with the alkylation routes. Similar formations of imido ligands from various nitrile ligands were published by Hidai et al. for Mo and W complexes.²⁴

In the synthesis, the starting complex $[\text{Mo}(\text{N}_2)_2(\text{depe})_2]$ is first protonated using trifluoromethanesulfonic acid (HOTf), which results in loss of one dinitrogen ligand followed by an

Scheme 2. Reaction Pathway To Synthesize 2-MeCN and 2-OTf



intramolecular redox process to obtain the Mo(IV)–hydrazido species $[\text{Mo}(\text{OTf})(\text{NNH}_2)(\text{depe})_2]\text{OTf}$ (**1**). When dissolved in acetonitrile, the triflate ligand of **1** is replaced by MeCN to form the intermediate complex $[\text{Mo}(\text{MeCN})(\text{NNH}_2)(\text{depe})_2]^{2+}$, which undergoes a fast proton shift if the base triethylamine is added in catalytic amounts. The deprotonated N_2 moiety is then displaced by triflate, and the acetonitrile is doubly protonated at the α -carbon to yield the imido complex $[\text{Mo}(\text{OTf})(\text{NEt})(\text{depe})_2](\text{OTf})$ (**2-OTf**), which is immediately transformed to $[\text{Mo}(\text{MeCN})(\text{NEt})(\text{depe})_2](\text{OTf})_2$ (**2-MeCN**) in acetonitrile.¹⁵

Complex **2-MeCN** obtained this way can be transformed to the triflate-analogue **2-OTf** if it is dissolved in THF. Exchange of the trans ligand (triflate against acetonitrile) was monitored by NMR and UV–vis spectroscopy. In the ^{19}F NMR spectra (Figure 1) the presence of a single triflate species for **2** in MeCN is indicated by the single signal at -79.4 ppm. In comparison, two different ^{19}F -containing species are detected

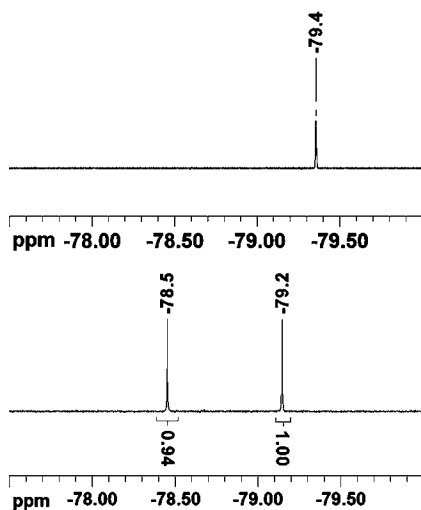


Figure 1. ^{19}F NMR spectra of **2-MeCN** in acetonitrile (top) and **2-OTf** in THF (bottom).

for **2** in THF with signals at -78.5 and -79.2 ppm. This can be taken as evidence for the presence of two equivalent, uncoordinated triflate anions in **2-MeCN**, whereas in **2-OTf** one triflate is coordinated and one triflate acts as a counterion, in agreement with the crystal structure (see below).²⁵

Exchange of the trans ligand also involves changes in the UV–vis spectrum of **2**. While **2** in MeCN shows a very broad absorption band at about 540 nm in acetonitrile, this band is blue shifted to 510 nm when **2** is dissolved in THF (Figure 2). Additionally, the band at 320 nm shifts to 330 nm and the shoulder at 380 nm disappears.

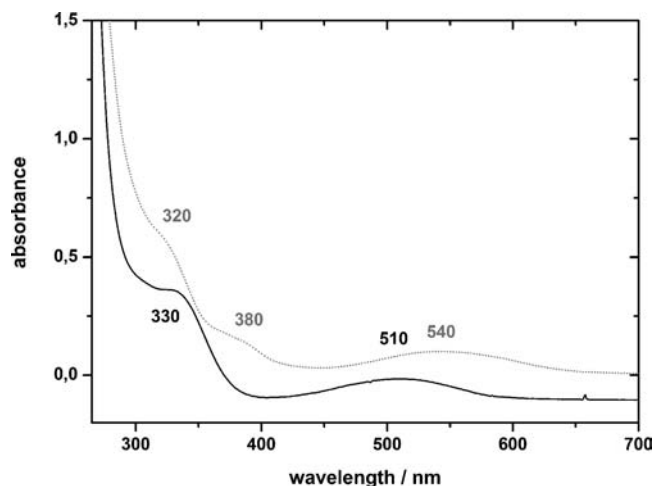


Figure 2. Comparison of UV–vis spectra of solutions (15 mM) of **2-MeCN** in acetonitrile (dotted line) and **2-OTf** in THF (solid line). Path length 0.1 cm.

B. Molecular Structure of 2-OTf. Pink, rod-shaped crystals of **2-OTf** could be obtained from a THF solution by slow evaporation of the solvent. Details of the crystal structure analysis can be found in Table 1. The compound crystallizes in the monoclinic non-centrosymmetric space group $P2_1$ with two molecules in the unit cell and all atoms in general positions. The molecular structure of **2-OTf** obtained from crystallo-

graphic analysis is shown in Figure 3; important bond distances and angles are collected in Table 2.

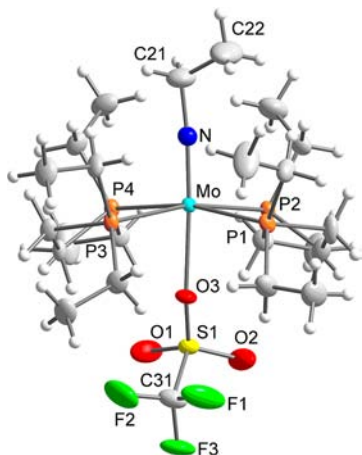


Figure 3. ORTEP presentation of the Mo(IV) ethylimido complex 2-OTf with labeling (displacement ellipsoids are drawn at the 50% probability level).

Table 2. Important Bond Distances [Angstroms] and Angles [degrees] of 2-OTf

	2-OTf
$d(\text{Mo}(1)-\text{N}(1))$	1.707(4)
$d(\text{Mo}(1)-\text{O}(3))$	2.278(3)
$d(\text{Mo}(1)-\text{P}(3))$	2.5157(10)
$d(\text{Mo}(1)-\text{P}(4))$	2.5271(11)
$d(\text{Mo}(1)-\text{P}(1))$	2.5334(10)
$d(\text{Mo}(1)-\text{P}(2))$	2.5422(10)
$d(\text{N}(1)-\text{C}(21))$	1.457(6)
$d(\text{C}(21)-\text{C}(22))$	1.459(9)
$\alpha(\text{N}(1)-\text{Mo}(1)-\text{O}(3))$	176.03(16)
$\alpha(\text{N}(1)-\text{Mo}(1)-\text{P}(3))$	95.51(13)
$\alpha(\text{O}(3)-\text{Mo}(1)-\text{P}(3))$	83.46(8)
$\alpha(\text{N}(1)-\text{Mo}(1)-\text{P}(4))$	94.35(13)
$\alpha(\text{O}(3)-\text{Mo}(1)-\text{P}(4))$	81.70(8)
$\alpha(\text{N}(1)-\text{Mo}(1)-\text{P}(1))$	98.35(13)
$\alpha(\text{O}(3)-\text{Mo}(1)-\text{P}(1))$	85.60(8)
$\alpha(\text{C}(21)-\text{N}(1)-\text{Mo}(1))$	174.9(4)
$\alpha(\text{N}(1)-\text{Mo}(1)-\text{P}(2))$	97.04(13)
$\alpha(\text{O}(3)-\text{Mo}(1)-\text{P}(2))$	84.01(8)
$\alpha(\text{P}(1)-\text{Mo}(1)-\text{P}(2))$	78.74(3)
$\alpha(\text{P}(4)-\text{Mo}(1)-\text{P}(2))$	99.26(3)
$\alpha(\text{P}(3)-\text{Mo}(1)-\text{P}(4))$	79.55(3)
$\alpha(\text{P}(3)-\text{Mo}(1)-\text{P}(1))$	99.63(3)
$\alpha(\text{P}(3)-\text{Mo}(1)-\text{P}(2))$	167.45(3)
$\alpha(\text{P}(4)-\text{Mo}(1)-\text{P}(1))$	167.29(3)
$\alpha(\text{S}(1)-\text{O}(3)-\text{Mo}(1))$	150.87(18)
$\alpha(\text{C}(21)-\text{N}(1)-\text{Mo}(1))$	174.9(4)
$\alpha(\text{N}(1)-\text{C}(21)-\text{C}(22))$	112.2(5)

All N–Mo–P angles of the octahedral complex are found to be larger than 90°. The metal center is thus positioned slightly above the P₄ plane, as observed before for related complexes like [MoCl(NEt)(dppe)₂](BPh₄)²⁶ or [MoCl(NMe)(dppe)₂](PF₆).²³ The Mo–N–C bond of the imido moiety is nearly linear (174.9°), as also found for the methylimido complex [MoCl(NMe)(dppe)₂](PF₆) (177.7°), but the bond angle is significantly larger than in [MoCl(NEt)(dppe)₂](BPh₄)

(162.0°/152.9°), where the ethyl ligand is disordered.¹³ Also, the N–C–C angle is larger in 2-OTf (112.2°) than in [MoCl(NEt)(dppe)₂](BPh₄) (104°). The Mo–N distance is 1.71 Å and thus slightly shorter than that determined for [MoCl(NEt)(dppe)₂](BPh₄) (1.73 Å).¹³

Looking at the differences between the structure shown in Figure 3 and known data, we conclude that the imido nitrogen in 2-OTf is best described as sp hybridized, while a larger sp² hybridization character of this atom applies to [MoCl(NEt)(dppe)₂](BPh₄). We attribute this difference to the electron donor properties of the ligand trans to the imido moiety: whereas a true triple bond exists between molybdenum and nitrogen in 2-OTf, the chlorido ligand of [MoCl(NEt)(dppe)₂](BPh₄) donates more electron density into the Mo–N bond than the triflate ligand, reducing the Mo–N bond order for [MoCl(NEt)(dppe)₂](BPh₄). In consequence, the Mo–N bond order is lower than three for [MoCl(NEt)(dppe)₂](BPh₄). Unfortunately, the Mo–N stretching band of 2-OTf cannot be observed in the vibrational spectra (data not shown). Otherwise, it would have been possible to confirm this conclusion spectroscopically, as we would expect a higher Mo–N vibration frequency for 2-OTf than the 916 cm^{−1} found previously for [MoCl(NEt)(dppe)₂](BPh₄).¹³ On the basis of similar considerations, we assume that the Mo–N(imide) bond of 2-MeCN has triple-bond character as well and its Mo–N–C(imide) angle is close to 180°. Further information on this issue is provided by the DFT calculations presented below.

C. Electrochemical Studies. 1. Electrochemistry of 2-OTf in THF. The cyclic voltammogram for reduction of 2-OTf in THF is shown in Figure 4. An irreversible reduction peak at

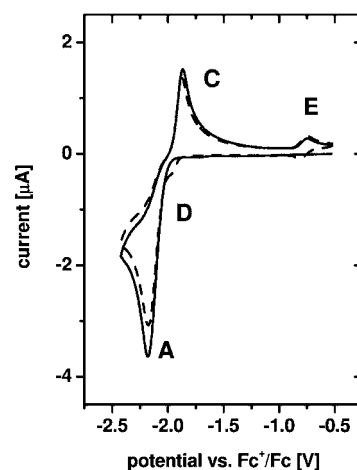


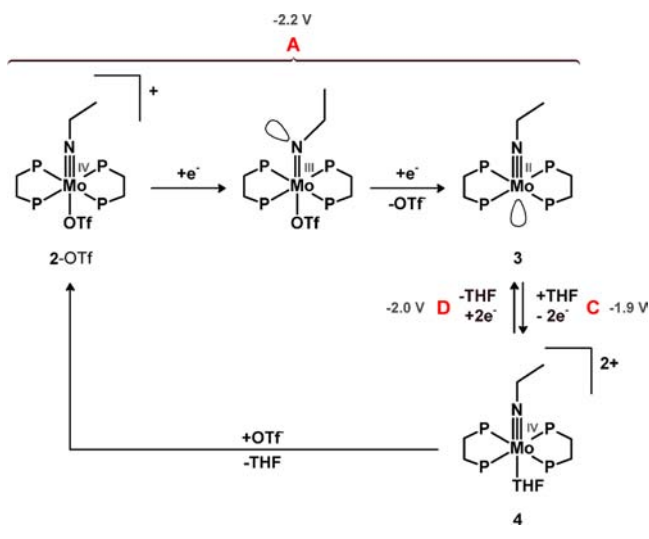
Figure 4. Cyclic voltammogram of [Mo(OTf)(NEt)(depe)₂]⁺ (2-OTf) in THF containing 0.1 M (NBu₄)(PF₆). Both the first (solid line) and the second (dotted line) scans are shown. Scan rate 0.1 V s^{−1}.

−2.2 V (marked A in Figure 4) is observed together with two consecutive reoxidation events at −1.8 (C) and −0.7 V (E), respectively. This reduction behavior closely resembles that previously reported by Alias et al. for [MoCl(NEt)(dppe)₂]⁺ (2-dppe-Cl) in DMF where reduction A was found at a potential of −2.2 V and reoxidation C at −1.6 V.¹³

In their work on the reduction of Mo(IV) ethylimido complexes 2-dppe-X with dppe and X = halide coligands, Alias et al. took the electrochemical events shown for 2-OTf in Figure 4, the results from coulometric measurements, and also the observation that C is found at the same position for both

the chlorido and the iodido complexes as strong indications for the reaction sequence shown in Scheme 1. As the electrochemical behavior of 2-OTf in THF very closely resembles that of 2-dppe-Cl in DMF (vide supra), the redox events of 2-OTf can be assigned in analogy to those of 2-dppe-X analyzed before. Event A in Figure 4 is therefore assigned to the stepwise two-electron reduction of 2-OTf to the five-coordinate complex $[\text{Mo}^{\text{II}}(\text{NEt})(\text{depe})_2]^+$ (3) via a short-lived Mo(III) intermediate (Scheme 3), and event C then represents the $2e^-$

Scheme 3. Reaction Pathways for $[\text{Mo}(\text{OTf})(\text{NEt})(\text{depe})_2]^+$ (2-OTf) in THF Following Its Electrochemical Reduction at -2.2 V (process A)



reoxidation of 3 accompanied by coordination of THF solvent to generate $[\text{Mo}^{\text{IV}}(\text{THF})(\text{NEt})(\text{depe})_2]^{2+}$ (4). Unfortunately, very slow electrolysis kinetics in THF solution made it impossible to verify these assignments by coulometry or EPR spectroscopy of bulk electrolyzed solutions. It can be seen that the current for event A is twice as large as for event C. Possible explanations can be found in the large peak split and thus the longer time for the reduction product to leave the volume close to the electrode through diffusion and in the possible decomposition of the reduction product. Moreover, there is the possibility that event A corresponds to a two-electron and event C to a one-electron process (see below). In addition to processes A and C, we also observe a second, very small reoxidation event E at a much higher potential of -0.7 V. Such a feature was not reported for $[\text{MoCl}(\text{NEt})(\text{dppe})_2]^+$ by Alias et al., who, however, did not extend their CV scans to this voltage region.

If two voltammograms of 2-OTf in THF are recorded consecutively, events A, C, and E are observed for both cycles with nearly unaltered peak currents. Two additional signals appear during the second CV cycle: (a) an additional reduction event D at -2.0 V, which was also observed for 2-dppe-X in DMF¹³ and assigned to reduction of the fraction of complex 4 that did not exchange the axial THF for the anionic ligand (in our case OTf⁻) to regenerate 2-OTf and (b) the completely reversible reduction ($\Delta E = 61$ mV) of the species generated before in event E.

Assignment of event D could be supported by a two-cycle CV recorded at a 10-fold faster sweep rate of 1 V s^{-1} (see Supporting Information, Figure S8), where it was found that the current measured for D relative to A increases significantly

for faster scan rates in the second cycle. This is in agreement with a less complete regeneration of 2-OTf from 4 if the time span for this reaction is reduced. Unlike for 2-dppe-X, it proved impossible to observe a single-electron-reduced Mo^{III} intermediate $(2\text{-OTf})^-$ by its reoxidation peak. Instead, reduction peak A was found to be completely irreversible both at higher scan rates of up to 1 V s^{-1} (see Supporting Information, Figure S8) and also at a reduced temperature of -50 °C (see Supporting Information, Figure S9). This indicates that loss of the axial triflate ligand occurs much faster for $(2\text{-OTf})^-$ than for the analogous reduced species $(2\text{-dppe-X})^-$. Reactions associated with events A, C, and D in the electrochemistry of 2-OTf in THF are collected in Scheme 3.

No obvious explanation for event E is provided by this scheme. In light of the results obtained in the following section an alternative mechanism can be formulated for the oxidative part of the cyclic voltammogram of 2-OTf in THF which involves a one-electron oxidation of 3 and does account for E. This is outlined at the end of the following section and summarized in Scheme 5 below.

2. Electrochemistry of 2-MeCN in MeCN. As shown in section A above, the complex $[\text{Mo}^{\text{IV}}(\text{MeCN})(\text{NEt})(\text{depe})_2]^{2+}$ (2-MeCN) with an acetonitrile ligand trans to the imido moiety is the dominant species present in an acetonitrile solution. The cyclic voltammogram for reduction of 2-MeCN at four different scan rates is shown in Figure 5. In comparison to reduction of

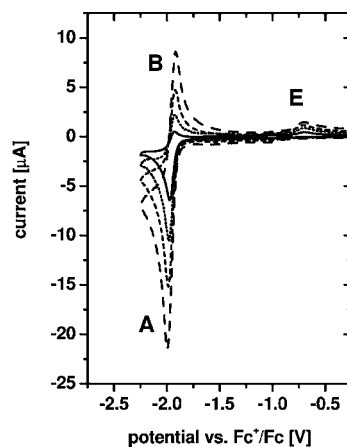
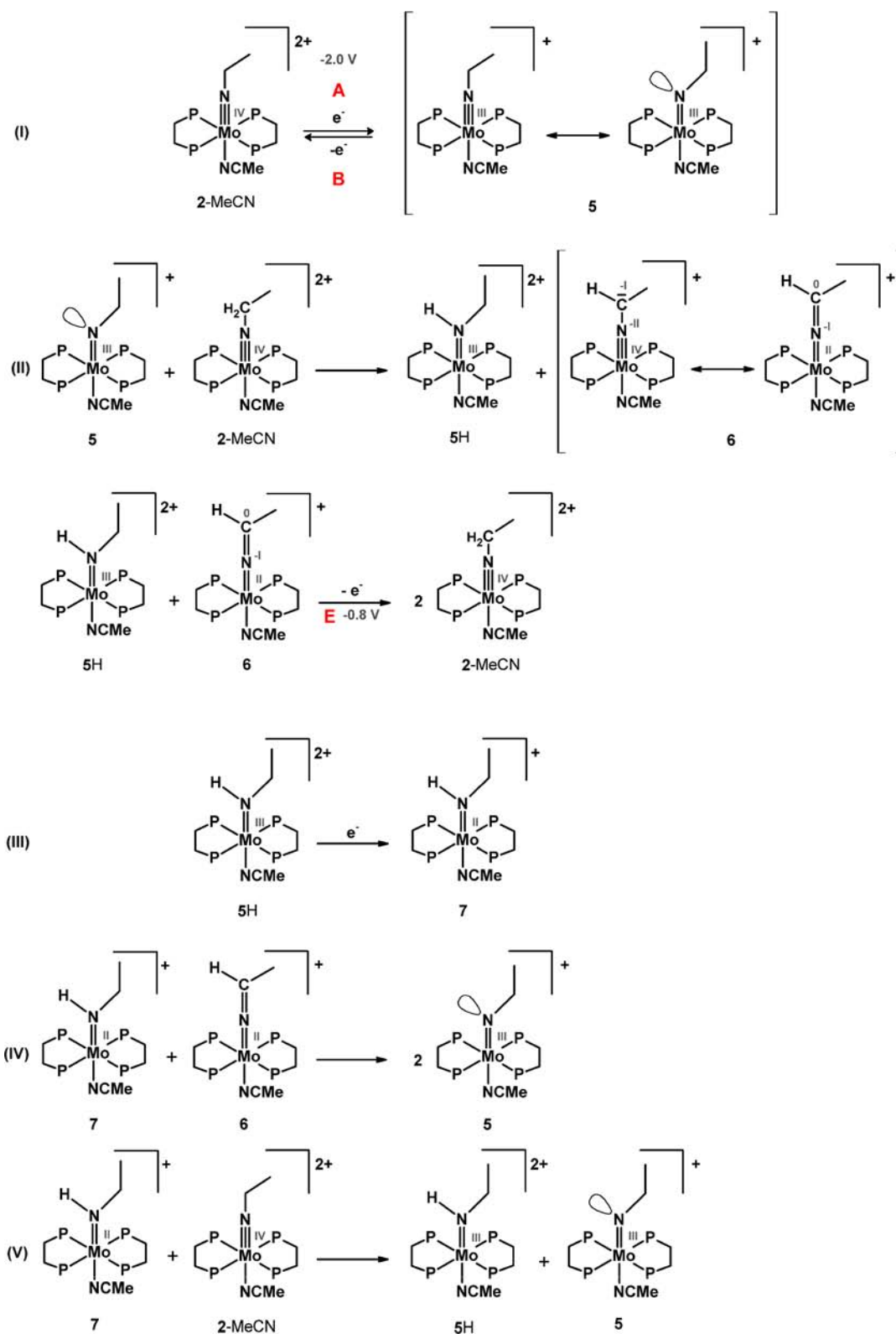


Figure 5. Cyclic voltammogram of $[\text{Mo}(\text{MeCN})(\text{NEt})(\text{depe})_2]^{2+}$ (2-MeCN) in MeCN containing 0.1 M $(\text{NBu}_4)(\text{PF}_6)$. Curves for scan rates of 0.1 (solid line), 0.25 (dotted line), 0.5 (short dashed line), and 1 V s^{-1} (long dashed line) are shown.

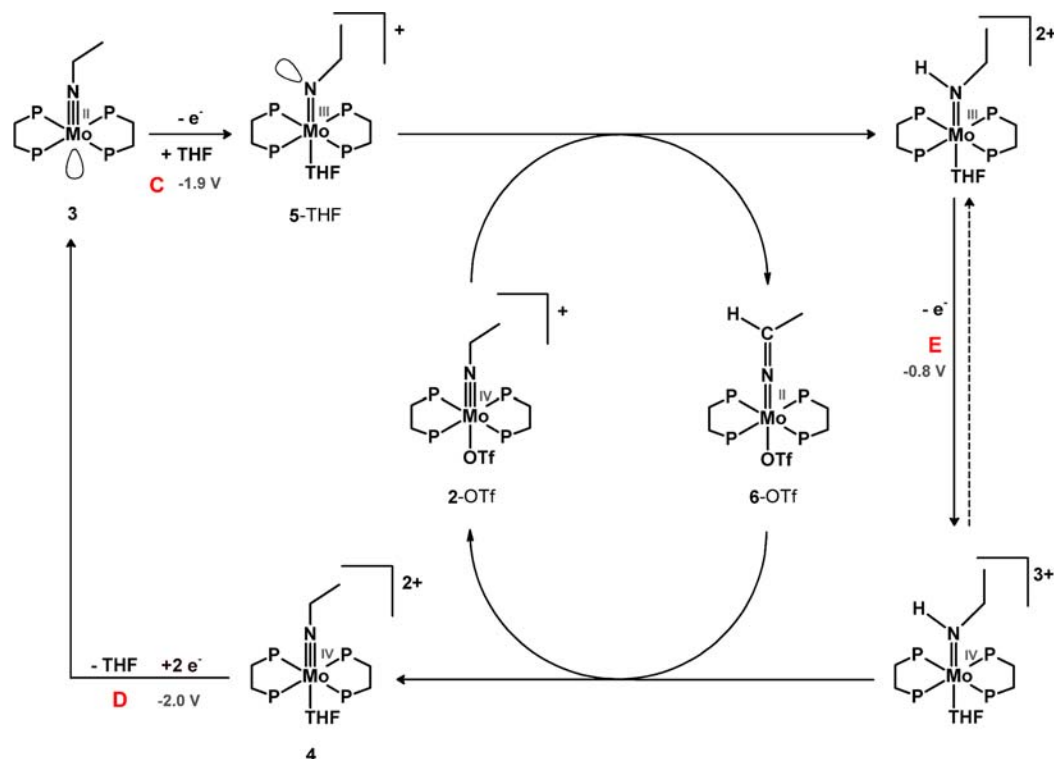
2-OTf in THF (Figure 4), the initial reduction peak A is found at a higher potential of -2.0 V for 2-MeCN. In addition, peak A is much sharper in appearance (see also Supporting Information, Figure S10, for a direct comparison), and already for a scan rate of 0.1 V s^{-1} the reoxidation peak B can be detected. With a peak split of $\Delta E = 60$ mV, it clearly belongs to event A. Peak B increases in relative intensity when compared to A at higher scan rates (Figure 5). This indicates that, unlike for 2-OTf, reduction of 2-MeCN does not result in immediate loss of the axial ligand. Instead, a reduced, six-coordinate intermediate with a significantly longer lifetime is formed, which can be reoxidized at B. Furthermore, reoxidation event C at a potential about 0.4 V higher than A (as found for $[\text{MoCl}(\text{NEt})(\text{dppe})_2]^+$ or 2-OTf) is completely absent at all scan rates. Event E can still be observed at -0.7 V with a very

Scheme 4. Reaction Pathways for $[\text{Mo}(\text{MeCN})(\text{NEt})(\text{depe})_2]^+$ (2-MeCN) in Acetonitrile Following Its Electrochemical Reduction at -2.0 V

small current but is not reversible, and a double-cycle CV does not show the appearance of the additional reduction event D detected before for 2-OTf (see Supporting Information, Figure S11).

Because of the more favorable properties of MeCN as electrolyte solvent in comparison to THF, a coulometric analysis of the reduction of 2-MeCN in acetonitrile could be carried out and revealed that one electron per 2-MeCN

Scheme 5. Redox Events for 2-OTf in THF with One-Electron Oxidation of the Five-Coordinate Mo(II) Complex 3



complex is transferred at a reduction potential of -2.2 V (see Supporting Information, Figure S12).

The presented results thus indicate that the reaction pattern found for 2-OTf in THF becomes greatly changed if complex 2-MeCN is studied in acetonitrile (Scheme 4). We conclude that, upon reduction, 2-MeCN *retains* the acetonitrile ligand in its coordination sphere and is transformed to the six-coordinate complex $[\text{Mo}^{\text{III}}(\text{MeCN})(\text{NEt})(\text{depe})_2]^+$ (5; cf. Scheme 4I). This species is, however, involved in follow-up reactions after its generation, as indicated by the scan-rate dependence of the electrochemical signal shown in Figure 5. We assume that it reacts with the parent Mo(IV) ethylimido complex to the Mo(III) ethylamido complex 5H and the Mo(II) azavinylidene complex 6 via an intramolecular redox reaction (Scheme 4II). To a small extent ($\sim 10\%$) formation of the azavinylidene complex has also been observed by Alias et al. after reduction of 2-dppe-Cl.¹³ It is well known from the literature that Mo(IV) alkylimido complexes exhibit C–H acidity at the α -C atom and can be deprotonated to Mo(II) azavinylidene complexes by strong bases.^{22a27} Event E then is assigned to reoxidation of 5H associated with a proton backtransfer to 6, regenerating two molecules of 2-MeCN (Scheme 4II, second line).

If formation of the Mo(IV) ethylimido complex 5H and the azavinylidene complex 6 was the end point of the reduction, only one-half an electron would be transferred per initial Mo(IV) ethylimido complex, which would be in contrast to the one-electron reduction of 2-MeCN evidenced by coulometry (vide supra). In agreement with the results obtained in the following sections (cyclic voltammetry of 2-MeCN and 2-OTf in the presence of protons) we thus anticipate that the Mo(III) amido complex 5H can receive a second electron at the applied potential and is transformed to the Mo(II) complex 7 (Scheme 4III). In a subsequent step, 7 and the azavinylidene complex 6 may comproportionate to reform the Mo(III) alkylidene

complex 5 as the ultimate product of the one-electron reduction of 2-MeCN (Scheme 4IV). This sequence of reactions is also supported by the spectroelectrochemical results presented below.

The reactivity of 5 evidenced in the cyclic voltammogram of 2-MeCN may also provide a clue to detection of event E in the CV of 2-OTf (vide supra). Specifically, if event C is not assigned to a two-electron oxidation of the five-coordinate Mo(II) complex 3 (as in Scheme 3) but to a one-electron oxidation of this species, a five-coordinate Mo(III) complex may be formed which can add a THF molecule to generate the six-coordinate Mo(III) complex 5-THF (Scheme 5). In analogy to the mechanistic scenario described for MeCN as solvent (Scheme 4II) this complex may deprotonate a molecule of 2-OTf to generate a Mo(III) ethylimido and an azavinylidene complex. One-electron oxidation of the ethylimido complex under reprotonation of the azavinylidene complex then would account for event E at -0.8 V (Scheme 5, right). In contrast to the acetonitrile system where this step is completely irreversible, reprotonation of the azavinylidene complex may be slow in THF, such that the Mo(IV) ethylimido complex has a sufficiently long lifetime to become one-electron reducible to its Mo(III) counterpart (Scheme 5, dotted arrow). Without further information, we cannot decide whether the two-electron oxidation of the Mo(II) complex 3 outlined in Scheme 3 or the one-electron oxidation shown in Scheme 5 is more realistic. Besides explaining the observation of event E, however, the latter scheme would also account for the fact that C exhibits about one-half of the peak height of A in Figure 4, as A would be associated with a two-electron reduction process whereas C would only represent a one-electron oxidation.

D. Spectroelectrochemical Studies. 1. UV–Vis Spectroelectrochemistry of 2-MeCN. The electrochemical results

presented in section C provided a strong indication that a single-electron-reduced Mo^{III} complex like [Mo^{III}(MeCN)(NEt)(depe)₂]⁺ (**5**) is formed by electrochemical reduction of 2-MeCN. Such a compound is unprecedented in molybdenum phosphine coordination chemistry, and we therefore studied this intermediate further using electrochemistry coupled to UV–vis and EPR spectroscopy. The changes of the UV–vis spectrum of 2-MeCN in acetonitrile recorded upon electrochemical reduction of the complex at –2.2 V in an optically transparent thin layer electrochemical (OTTLE) cell (see Supporting Information, Figure S4) are shown in Figure 6.

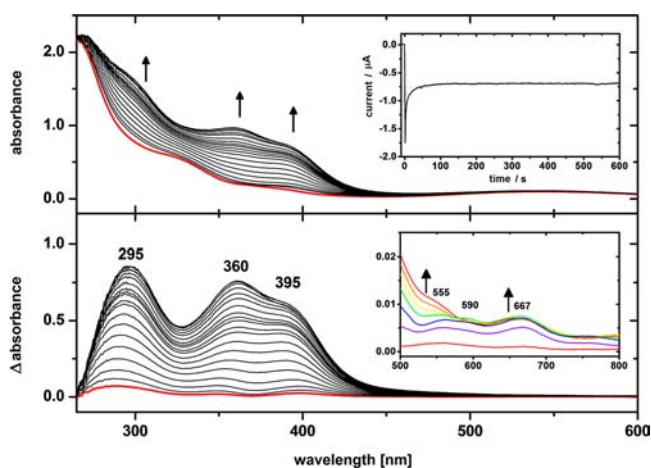


Figure 6. (Top) Changes of the UV–vis spectrum of 2-MeCN in acetonitrile recorded during an electrochemical reduction at –2.2 V inside an OTTLE cell. Spectra are shown for a total electrolysis time of 600 s at 30 s intervals. (Inset) Chronoamperometric detection of the reduction current. (Bottom) Difference spectra obtained from the data above by subtraction of the initial spectrum measured at $t = 0$ s. (Inset) Formation of the weak d–d band at higher wavelengths.

Profound changes of the UV–vis spectrum are observed, especially for the spectral range from 270 to 450 nm, as the solution changes its color during electrolysis from purple via red to yellow. Formation of three strong new absorption bands is detected, which are positioned at 295, 360, and 395 nm, respectively. In addition, a very weak new band at 667 nm appears in the spectral region characteristic of d–d transitions (Figure 6, inset). Because electrolysis in the OTTLE cell is purely diffusion controlled, the electrochemical reactions take place with much slower kinetics than found for a normal chronoamperometry setup. In addition, the processes do not reach a defined end point even within 10 min as the thin layer region of the cell is in contact with a much larger solution reservoir at the top of the cell (see Supporting Information, Figure S4). From there, unreduced 2-MeCN can diffuse toward the electrode grid over time (and thus into the UV–vis spectrometer beam), while product can also be lost from the reaction volume (see I vs t plot in Figure 6, inset of top figure). Nevertheless, it is possible to observe the nearly complete reversibility of the reduction reaction by UV–vis spectroscopy: if the solution obtained after 10 min of electrochemical reduction is reoxidized at a potential of 0 V, the initial UV–vis spectrum is obtained again (see Supporting Information, Figure S13).

Information with respect to the nature of the reduced species generated and observed in the spectroelectrochemical cell is

provided by Scheme 4 along with the TDDFT calculations presented below. Importantly, these calculations predict intense transitions in the near-UV region for the Mo(III) ethylimido and Mo(II) azavinylidene complexes **5** and **6**, respectively, whereas the Mo(II) and Mo(III) ethylamido complexes **5H** and **7** should be transparent in this region. These predictions are also supported by the spectroelectrochemical measurements in the presence of a proton source where the intense near-UV transitions are suppressed (see below). According to Scheme 4, one-electron reduction of 2-MeCN in acetonitrile leads to the Mo(II) ethylamido complex **7** and the azavinylidene complex **6** which in a last step may recombine to the Mo(III) ethylimido complex **5**. One-electron reduction of 2-MeCN may thus ultimately lead to a mixture of complexes **5**, **6**, and **7**. Closer inspection of the growth of the absorption bands in Figure 6 and, in particular, their disappearance upon reoxidation (Supporting Information, Figure S13) reveals that they are due to two components. On the basis of the TDDFT calculations presented below these can be assigned to the Mo(III) alkylnitrene complex **5** and the Mo(II) azavinylidene complex **6**.

2. EPR Spectroelectrochemistry of 2-MeCN. In an approach similar to the UV–vis experiments, the reduced form of 2-MeCN was also generated inside an EPR tube using a special two-electrode setup to perform in situ EPR spectroscopy (see Supporting Information, Figure S5).²⁰ Figure 7 shows the EPR spectrum of **5** at room temperature, obtained after electrochemical reduction of 2-MeCN, which itself is EPR silent.

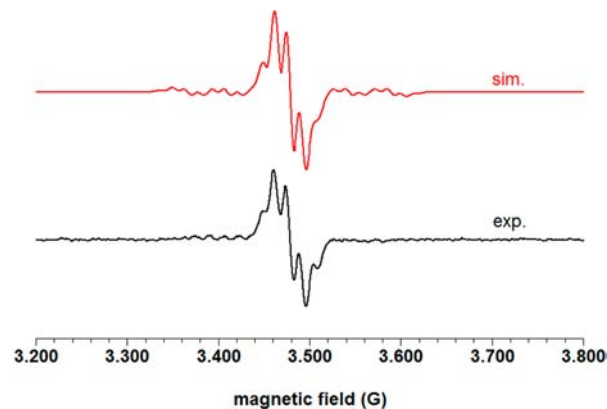


Figure 7. Room-temperature X-band EPR spectrum generated in situ by electrochemical reduction of 2-MeCN in solution (acetonitrile). EPR parameters: microwave frequency, 9.78 GHz; modulation amplitude, 4 G; modulation frequency, 100 kHz. (Red line) Isotropic simulation of the spectrum using the parameters $g_{\text{iso}} = 2.0091$, $A_{\text{iso}}(^{95/97}\text{Mo}) = 43.32$ G, $A_{\text{iso}}(^{31}\text{P}) = 12.73$ G (4 P), line width = 13.25 G. Figure S6 in the Supporting Information shows the appertaining simulation with anisotropic parameters.

The spectrum consists of a 200 G wide five-line signal centered at 3480 G ($g = 2.01$). To the best of our knowledge, there is only one report of a comparable EPR spectrum for a molybdenum phosphine complex exhibiting at least related spectral features, which was recorded for the molybdenum(V) compound [Mo^VCl(NMe)(dpppe)₂]²⁺.²³ The fact that the spectrum resulting from reduction of a molybdenum(IV) precursor is similar to that of a molybdenum(V) complex indicates that the reduction product obtained here, like [Mo^VCl(NMe)(dpppe)₂]²⁺, can be described as an $S = 1/2$ spin system coupling to four magnetically equivalent ³¹P nuclei

($I = 1/2$) of the depe ligands as well as the $^{95}\text{Mo}/^{97}\text{Mo}$ metal centers (both $I = 5/2$, natural abundance 15.9% and 9.6%, respectively). As can be seen in Figure 6, a good agreement between simulation and experiment is reached if isotropic hyperfine coupling constants of 12.73 and 43.32 G are used for the interaction of the unpaired electron with the ^{31}P and $^{95/97}\text{Mo}$ nuclear spins, respectively. In contrast to the reported EPR spectrum of $[\text{Mo}^{\text{V}}\text{Cl}(\text{NMe})(\text{dppe})_2]^{2+}$,²³ the hyperfine coupling with ^{14}N and the alkyl protons (literature values: $A_{\text{iso}}(^{14}\text{N}) = 3.4$ G, $A_{\text{iso}}(^1\text{H}) = 3.6$ G)²³ is not resolved in the EPR spectrum of reduced 2-MeCN due to the relatively large line width (Figure 7) and the low intensity compared with Mo(V) complexes. Moreover, the phosphorus hyperfine splitting parameter found for the latter species (12.73 G) is markedly smaller than the one obtained for $[\text{Mo}^{\text{V}}\text{Cl}(\text{NMe})(\text{dppe})_2]^{2+}$ ($A_{\text{iso}}(\text{P}) = 20.2$ G).

Taken together, the results from EPR spectroelectrochemistry clearly support our result that reduction of 2-MeCN in acetonitrile solution indeed yields an unusual, single-electron-reduced $S = 1/2$ Mo(III) complex at room temperature in solution. The absence of a significant nitrogen hyperfine coupling and the presence of four equivalent ^{31}P nuclei, however, speak against the assignment of this EPR spectrum to the unprotonated, bent Mo(III) alkylidene complex **5**. It rather appears that this spectrum is associated with the Mo(III) ethylamido complex **5H** which has a higher symmetry and lower nitrogen contribution to its SOMO as compared to the alkylidene complex **5** (see below). The fact that not **5** but **5H** is detected in the EPR experiment can be explained by a comproportionation reaction between the Mo(II) ethylidene complex **7** formed electrochemically in the vicinity of the cathode at the applied potential (cf. Scheme 4III; see also Supporting Information Figure S5 for the cell geometry) and parent Mo(IV) complex 2-MeCN being present in the cell, forming **5H** and **5** (Scheme 4V). **5** then reacts with further 2-MeCN to generate additional **5H** and the azavinylidene complex **6** (cf. Scheme 4II), the latter being EPR silent.

E. Electrochemistry and Spectroelectrochemistry of 2-OTf and 2-MeCN in the Presence of a Proton Source. To obtain further insight into the elementary steps involved in the reduction of 2-OTf or 2-MeCN, electrochemical measurements were also performed in the presence of a weak acid. Phenol (PhOH) has been used as H^+ donor in this context before because the molecule combines significant acidity with electrochemical stability, making reductions up to -2.2 V without H_2 evolution possible (see Supporting Information, Figure S14).¹³

The effect of the proton source phenol on the electrochemistry of 2-OTf is demonstrated in Figure 8, left. While the primary reduction event at -2.2 V is not affected in its potential by PhOH, the reoxidation peak at -1.6 V completely disappears in the presence of PhOH and simultaneously new reoxidation events at -1.53 and -0.82 V are observed. An even more profound change is found for 2-MeCN, where partial reversibility of the reduction at -2.0 V found in neat acetonitrile is totally absent in phenol-containing acetonitrile, even at fast scan rates (Figure 8, right, and Supporting Information, Figure S15). Instead, two new reoxidation peaks are observed at -1.55 and -0.84 V, quite similar to those observed for 2-OTf.

Of key relevance in the context of N_2 reduction, the results demonstrate that the centrally important combination of metal reduction and nitrogen-ligand protonation is observed here for

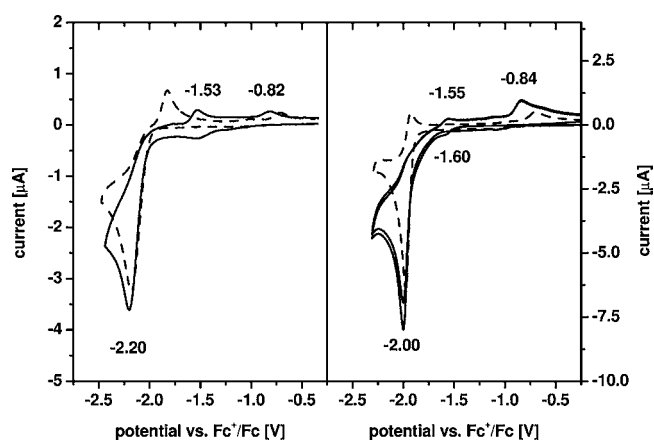


Figure 8. Cyclic voltammograms of 2-OTf (left, 1 mM in THF) and 2-MeCN (right, 1 mM in MeCN) in the absence (dotted lines) and presence (solid lines) of 1 equiv of phenol.

mononuclear molybdenum(IV) nitrido/imido complexes with depe coligands as well. Specifically, reductions of 2-OTf or 2-MeCN render Mo(III) imido complexes which are basic enough to abstract a proton from PhOH, generating Mo(III) amido species which are further reduced to Mo(II) amido species (Scheme 6). This, in particular, explains the disappearance of the reversible Mo(III) \rightarrow Mo(IV) oxidation peak of 2-MeCN in acetonitrile (B in Figure 5). Once phenolate anions are formed, PhO^- displaces the ligands axial to the imido/amido moiety, thus generating $[\text{Mo}^{\text{III}}(\text{OPh})(\text{HNet})(\text{depe})_2]^+$ (**5H-OPh**) or $[\text{Mo}^{\text{II}}(\text{OPh})(\text{HNet})(\text{depe})_2]$ (**7-OPh**). This ligand exchange is suggested by the similarity of the CVs for 2-MeCN and 2-OTf in the presence of phenol. Reoxidation of the formed Mo(II) amido species takes place at ~ -1.6 V (C) and reoxidation of the Mo(III) amido species at ~ -0.8 V (E; cf. Figure 8 and Scheme 6I).

In order to obtain information on the nature of the transient species involved in this reaction sequence, reduction of 2-MeCN was also performed in the UV-vis spectroelectrochemical cell in the presence of phenol and acetonitrile as solvent. As can be clearly seen in Figure 9, formation of intense new absorption bands in the near-UV region (as shown in Figure 6) is suppressed. This suggests that now Mo(III) and Mo(II) amido complexes are generated which lack intense absorption bands in the near-UV region (see below). The Mo(III) amido complex **5-OPh**, however, is predicted to exhibit an intense phenolate \rightarrow metal LMCT band at 600 nm (see below), which is not observed experimentally and is not predicted for the Mo(II) alkylamido complex **7-OPh**. We thus further conclude that the final product of the reduction of **2** in the presence of phenol is in fact the Mo(II) amido complex **7-OPh**, in agreement with Scheme 6I.

Reduction of 2-MeCN in acetonitrile containing phenol was also monitored by EPR spectroelectrochemistry. The obtained Mo(III) EPR spectrum (Figure 10) is qualitatively similar to that obtained in neat MeCN which was assigned to the Mo(III) ethylamido complex **5H** (vide supra). The spectrum obtained in the presence of phenol, however, exhibits a 44% larger hyperfine splitting as compared to **5H**. The results of cyclic voltammetry (Scheme 6I) suggest that the relevant Mo(III) species now is the ethylamido complex **5H-OPh**. The fact that a persistent concentration of this species is detected in the EPR experiment can again be explained by a comproportionation reaction between the Mo(II) ethylidene complex (now **7-OPh**)

Scheme 6. Reduction of 2-MeCN in the Presence of Phenol

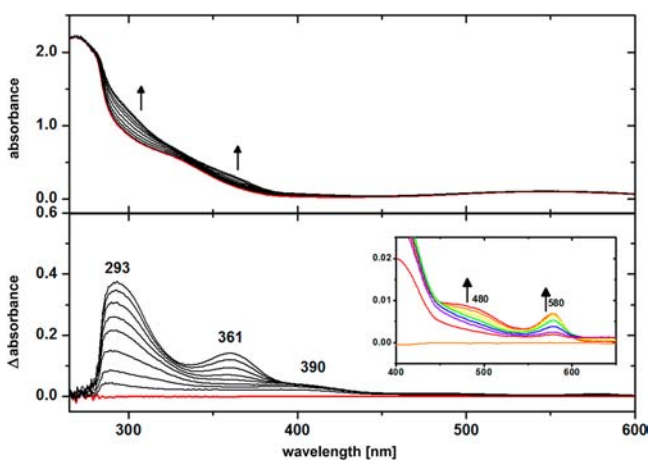
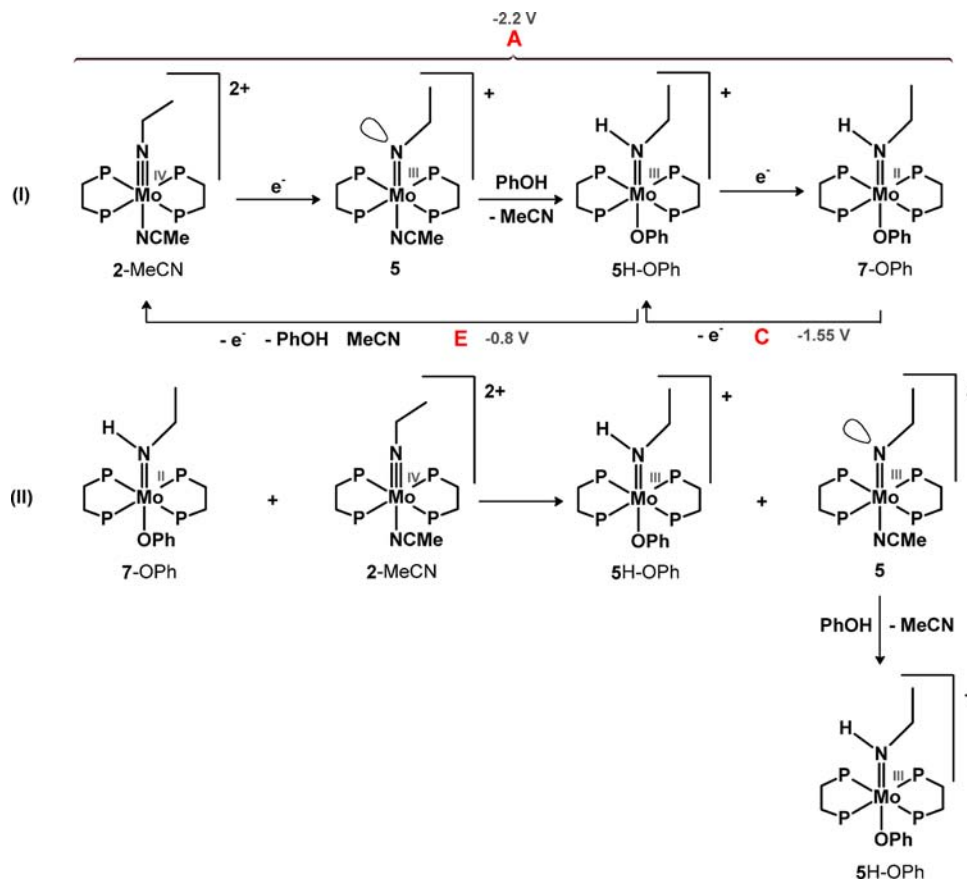


Figure 9. (Top) UV-vis spectra recorded during reduction of 2-MeCN in acetonitrile containing 0.1 M $(\text{NBu}_4)(\text{PF}_6)$ in the presence of 1 equiv of phenol at a potential of -2.2 V . Over a period of 345 s, 24 spectra were measured. For the first 165 s every second spectrum is shown and for the rest every fourth. (Bottom) Difference spectra of the reduction. For the first 165 s every second spectrum is shown and for the rest every fourth.

formed electrochemically in the vicinity of the cathode at the applied potential and parent Mo(IV) complex 2-MeCN being present in the cell, leading to 5H-Oph and 5 (Scheme 6II). The alkylnitrene complex 5 is in turn protonated by phenol to give 5H-Oph.

In summary, we find that the reduction pathways of 2-OTf and 2-MeCN are greatly changed if protons are present in

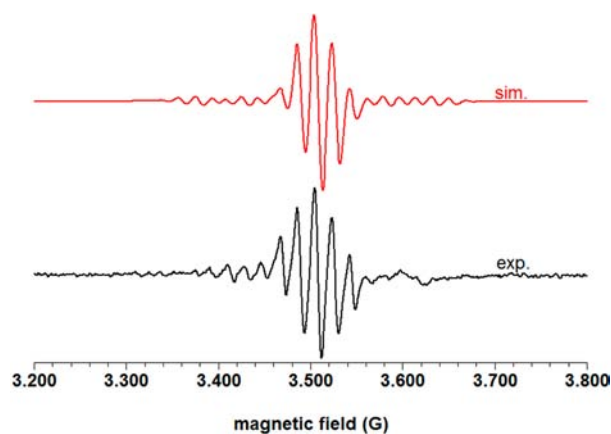


Figure 10. Room-temperature X-band EPR spectrum obtained in situ by electrochemical reduction of 2-MeCN in acetonitrile solution in the presence of phenol. EPR parameters: microwave frequency, 9.78 GHz; modulation amplitude, 4 G; modulation frequency, 100 kHz. (Red line) Isotropic simulation of the spectrum using the following parameters: $g_{\text{iso}} = 1.9916$, $A_{\text{iso}}(^{95/97}\text{Mo}) = 50.57\text{ G}$, $A_{\text{iso}}(^{31}\text{P}) = 18.34\text{ G}$ (4 P), line width 11.50 G. Figure S7 in the Supporting Information shows the appertaining simulation with anisotropic parameters.

solution. However, the first electron-transfer process seems largely unaffected by the presence of the proton source. This indicates that an initial one-electron reduction is needed first for the Mo(IV) ethylimido complexes 2 to create a sufficiently basic Mo(III) alkylnitrene species for proton transfer to occur. After protonation, a second electron can be transferred

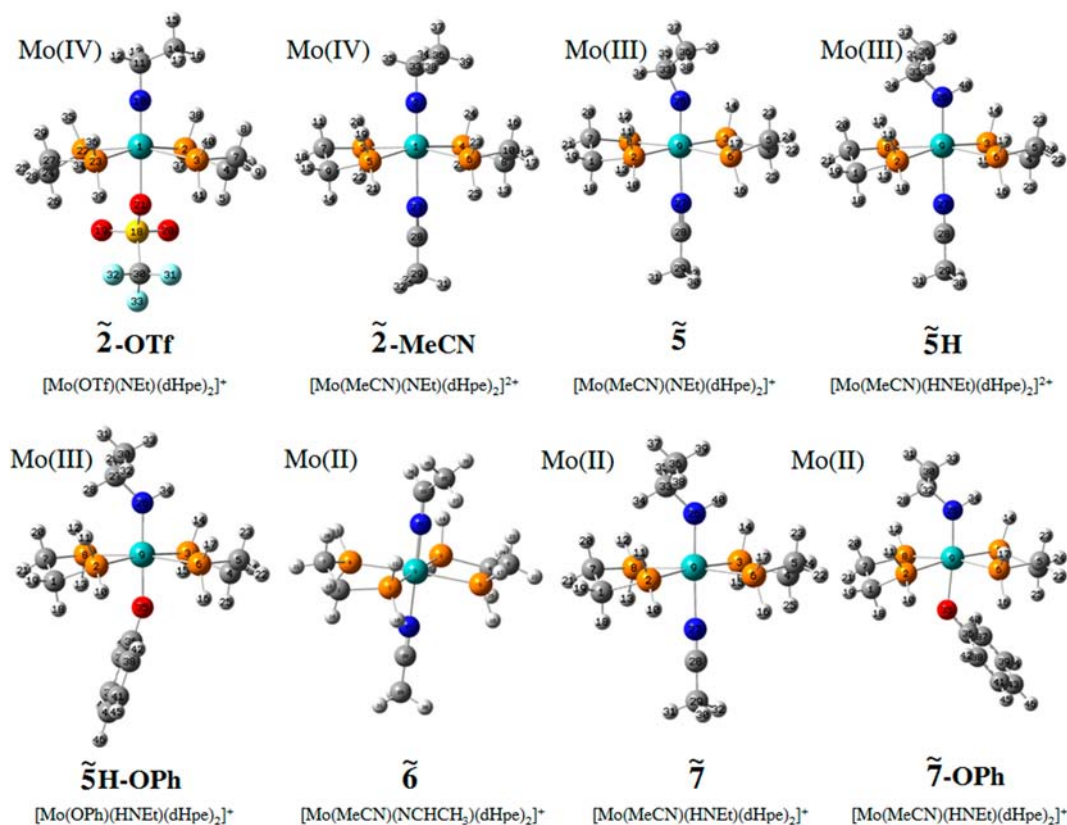


Figure 11. Overview of geometry-optimized structures of the simplified complexes obtained by DFT calculations.

immediately at the same potential, forming a Mo(II) amido complex.

F. DFT and TDDFT Studies. 1. *2-OTf* and *2-MeCN*. In order to calibrate the DFT calculations for treatment of the new Mo(III)/Mo(II) intermediates **5**, **5H**, **5H-OPh**, **6**, **7**, and **7-OPh**, DFT calculations of the Mo(IV) precursors **2-OTf** and **2-MeCN** were performed first. Truncated versions of the ligands ($\text{dHpe} = \text{H}_2\text{PCH}_2\text{CH}_2\text{PH}_2$) were used, and the resulting geometry-optimized structures are shown in Figure 11.

The geometry-optimized structure of **2-OTf** (Figure 11, top left) correlates very well with the one obtained from X-ray crystallography of **2-OTf** (vide supra), which we take as strong support for the good quality of the applied theoretical description. The Mo–N bond length is 1.74 Å (X-ray data for **2-OTf** 1.71 Å). The Mo–N–C angle is 179.7° (**2-OTf** 174.9°), the N–Mo–C angle 175.6° (**2-OTf** 176.0°), and the N–C–C angle 112.5° (**2-OTf** 112.2°). The MO scheme and denominations of the molecular orbitals are given in the Supporting Information. The HOMO of **2-OTf** is the metal–ligand nonbonding orbital d_{xy} which is doubly occupied; the LUMO is contained in the d_{xz}/d_{yz} pair of orbitals which are empty.

On the basis of the optimized geometry of **2-OTf**, we also performed TDDFT calculations. A comparison between the calculated and the experimental UV–vis spectrum of **2-OTf** is shown in Figure 12. The most important calculated transition energies are collected in Table 3.

For the HOMO \rightarrow LUMO transition ($d_{xy} \rightarrow d_{xz-p_x}(\text{NEt})$; cf. Supporting Information) an energy of 477 nm is obtained by TDDFT, which has to be compared with the observed transition at 510 nm. Furthermore, a weak transition is

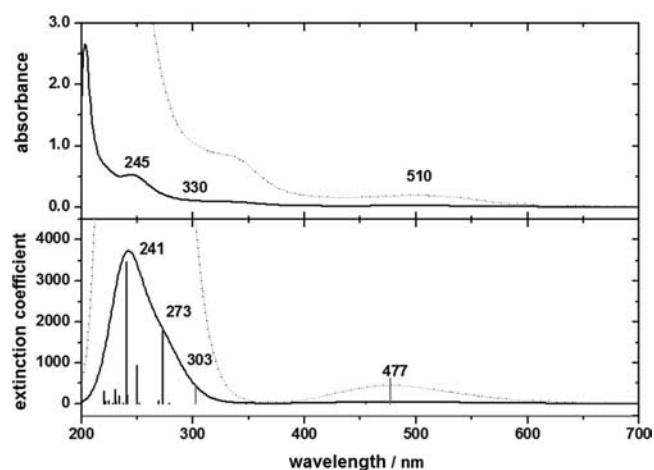


Figure 12. Comparison of UV–vis spectra of **2-OTf** in KBr (top) and **2-OTf** (bottom). Spectra enlarged by a factor of 10 are drawn in dotted lines. Intensities of the lines at 477 and 303 nm in the calculated spectrum were also multiplied by 10.

calculated at 303 nm for the $d_{xy} \rightarrow d_{z^2-p}(\text{Mo})$ ligand-field transition. No intensity is determined for the $d_{xy} \rightarrow d_{x^2-y^2-p}(\text{P})$ transition. A number of transitions from the lower occupied orbitals (99)–(104) into the two unoccupied $d_{xz-p_x}(\text{NEt})$ and $d_{yz-p_y}(\text{NEt})$ orbitals (cf. Supporting Information) are calculated between 270 and 230 nm, the most intense being the one at 273 nm. Another intense transition is calculated at 241 nm and assigned to the transition $p(\text{P}) \rightarrow d_{x^2-y^2-p}(\text{P})$. All these intense bands thus correspond to ligand to metal charge-transfer transitions.

Table 3. Electronic Transitions of $\tilde{2}$ -OTf from TDDFT Calculations

no.	energy/ nm	oscillator strength	transition	type of transition
1	477	0.0011	$d_{xy}\langle 105 \rangle \rightarrow d_{xz_p_x}\langle \text{NEt} \rangle \langle 106 \rangle$	LF
4	303	0.0008	$d_{xy}\langle 105 \rangle \rightarrow d_{z^2_p}\langle \text{P} \rangle \langle 108 \rangle$	LF
6	273	0.0314	$p\langle \text{OTf} \rangle \langle 104 \rangle \rightarrow d_{xz_p_x}\langle \text{NEt} \rangle \langle 106 \rangle$	LMCT
7	269	0.0013	$p\langle \text{P} \rangle \langle 103 \rangle \rightarrow d_{xz_p_x}\langle \text{NEt} \rangle \langle 106 \rangle$	LMCT
9	250	0.0165	$p\langle \text{P} \rangle \langle 103 \rangle \rightarrow d_{yz_p_y}\langle \text{NEt} \rangle \langle 107 \rangle$	LMCT
10	242	0.0036	$p_y\langle \text{NEt} \rangle d_{yz}\langle 99 \rangle \rightarrow d_{yz_p_y}\langle \text{NEt} \rangle \langle 107 \rangle$	LMCT
11	241	0.0608	$d_{xy}\langle 105 \rangle \rightarrow p\langle \text{Mo} \rangle \langle 110 \rangle$	

The geometry-optimized structure of $\tilde{2}$ -MeCN is also shown in Figure 11. Its electronic structure is very similar to that of $\tilde{2}$ -OTf. The theoretical and experimental UV-vis spectra for $\tilde{2}$ -MeCN and 2-MeCN are shown in Figure 13 for direct comparison; the calculated transition energies are collected in Table 4.

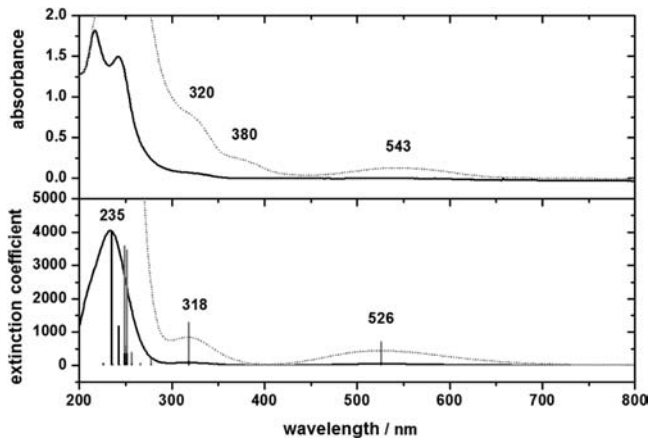


Figure 13. Comparison of UV-vis spectra of 2-MeCN in KBr (top) and $\tilde{2}$ -MeCN (bottom). Spectra multiplied by 10 are drawn in dotted lines. Intensities of the lines at 526 and 318 nm in the calculated spectrum were also multiplied by 10.

For the HOMO \rightarrow LUMO transition ($d_{xy} \rightarrow d_{xz_p_x}\langle \text{NEt} \rangle$; cf. Supporting Information), a wavelength of 526 nm is obtained which compares well with the observed band at 543 nm. Very little intensity is predicted for the $d_{xy} \rightarrow d_{x^2-y^2_p}\langle \text{P} \rangle$ and $d_{xy} \rightarrow d_{yz_p_y}\langle \text{NEt} \rangle$ transitions. One band at 318 nm is assigned to the ligand-field transitions $d_{xy} \rightarrow d_{z^2_p}\langle \text{Mo} \rangle$ and $d_{xy} \rightarrow d_{x^2-y^2_p}\langle \text{P} \rangle$. Thus, this band has lower energy than calculated for $\tilde{2}$ -OTf. Furthermore, ligand \rightarrow metal charge-transfer (LMCT) transitions from the occupied orbitals $\langle 75 \rangle - \langle 79 \rangle$ (corresponding to the bonding linear combinations $p_x\langle \text{NEt} \rangle d_{xz}$ and $p_y\langle \text{NEt} \rangle d_{yz}$ as well as $p\langle \text{P} \rangle p\langle \text{Mo} \rangle$) into the unoccupied $d_{xz_p_x}\langle \text{NEt} \rangle$ and $d_{yz_p_y}\langle \text{NEt} \rangle$ orbitals are obtained at 252 and 243 nm. Metal to ligand charge-transfer (MLCT) transitions, on the other hand, are calculated for $d_{xy} \rightarrow p_x\langle \text{MeCN} \rangle p\langle \text{Mo} \rangle$ and $d_{xy}\langle 79 \rangle \rightarrow p\langle \text{Mo} \rangle p_x\langle \text{MeCN} \rangle$ at 248 and 235 nm, respectively.

2. Mo(III) Alkylidene Complex 5. Having calibrated the DFT calculations on the basis of the results for complexes 2-OTf and 2-MeCN we wanted to obtain further insight into the

Table 4. Electronic Transitions of $\tilde{2}$ -MeCN from TDDFT Calculations

no.	energy/ nm	oscillator strength	transition	type of transition
1	526	0.0011	$d_{xy}\langle 79 \rangle \rightarrow d_{xz_p_x}\langle \text{NEt} \rangle \langle 80 \rangle$	LF
2	488	0.0000	$d_{xy}\langle 79 \rangle \rightarrow d_{yz_p_y}\langle \text{NEt} \rangle \langle 81 \rangle$	LF
3	346	0.0001	$d_{xy}\langle 79 \rangle \rightarrow d_{x^2-y^2_p}\langle \text{P} \rangle \langle 83 \rangle$	LF
4	318	0.0020	$d_{xy}\langle 79 \rangle \rightarrow d_{z^2_p}\langle \text{Mo} \rangle p\langle \text{P} \rangle \langle 82 \rangle$	LF
5	278	0.0003	$p_y\langle \text{NEt} \rangle d_{yz}\langle 76 \rangle \rightarrow d_{xz_p_x}\langle \text{NEt} \rangle \langle 80 \rangle$	LMCT
7	257	0.0006	$p\langle \text{P} \rangle \langle 78 \rangle \rightarrow d_{xz_p_x}\langle \text{NEt} \rangle \langle 80 \rangle$	LMCT
8	252	0.0054	$p\langle \text{P} \rangle \langle 78 \rangle \rightarrow d_{yz_p_y}\langle \text{NEt} \rangle \langle 81 \rangle$	LMCT
9	250	0.0009	$p_x\langle \text{NEt} \rangle d_{xz}\langle 75 \rangle \rightarrow d_{xz_p_x}\langle \text{NEt} \rangle \langle 80 \rangle$	LMCT
10	248	0.0057	$d_{xy}\langle 79 \rangle \rightarrow p_x\langle \text{NCMe} \rangle p\langle \text{Mo} \rangle \langle 84 \rangle$	MLCT
12	243	0.0183	$p\langle \text{P} \rangle p\langle \text{Mo} \rangle \langle 77 \rangle \rightarrow d_{xz_p_x}\langle \text{NEt} \rangle$	LMCT
14	235	0.0622	$d_{xy}\langle 79 \rangle \rightarrow p\langle \text{Mo} \rangle p_x\langle \text{NCMe} \rangle \langle 86 \rangle$	

electronic structures and the spectroscopic properties of the Mo(III) and Mo(II) complexes obtained by reduction of 2-OTf and 2-MeCN. To this end the Mo(III) ethylimido complex **5** was investigated first. Geometry optimization of the Mo(III) model $[\text{Mo}(\text{MeCN})(\text{NEt})(\text{PH}_2\text{CH}_2\text{CH}_2\text{PH}_2)_2]^+$ (**5**) leads to the structure shown in Figure 11. Importantly, the Mo-N-C angle in **5** is reduced from 180° (as calculated for $\tilde{2}$ -MeCN) to 154.8° . The Mo-N(imide) bond is elongated by about 0.1–1.82 Å (X-ray data for 2-OTf 1.71 Å, calculation for $\tilde{2}$ -MeCN 1.74 Å), which is due to occupation of a π -antibonding linear combination of imido p and molybdenum d orbitals. The Mo-N(acetonitrile) bond length of 2.32 Å is slightly shorter than the one calculated for $\tilde{2}$ -MeCN (2.38 Å). Overall, DFT geometry optimization of **5** supports a bent structure of **5** and thus formulation of this species as an alkylidene complex. The MO scheme and designations of the molecular orbitals are given in the Supporting Information. Importantly, the single unpaired electron resides in a π -antibonding orbital of mixed molybdenum d nitrogen p character which is designated as $d_{xz_p_x}\langle \text{NEt} \rangle$.

On the basis of TDDFT calculations, the theoretical UV-vis spectrum shown in Figure 14 is obtained. The corresponding electronic transitions are listed in Table 5. Comparison of the UV-vis spectrum with the one obtained during electrochemical reduction of 2-MeCN (Figure 9) with the theoretically derived spectrum is shown in Figure 14 (bottom). It can be seen that the calculation gives one high-intensity absorption feature in the near-UV region, i.e., at 400 nm. This band is associated with the $d_{xz_p_x} \rightarrow \pi^*(\text{MeCN})$ transition, i.e., a transition from the SOMO of **5** into the π^* orbital of the coordinated nitrile ligand. Clearly, this transition is absent for the Mo(IV) precursor 2-MeCN and only appears after one-electron reduction of this complex.

Mulliken spin densities of **5** show an equal contribution of the single electron over the Mo center and the nitrogen atom of the NEt ligand (Mo 0.43, N(NEt) 0.45). The spin density at the P atoms, in contrast, is quite low (P(mean) 0.004).

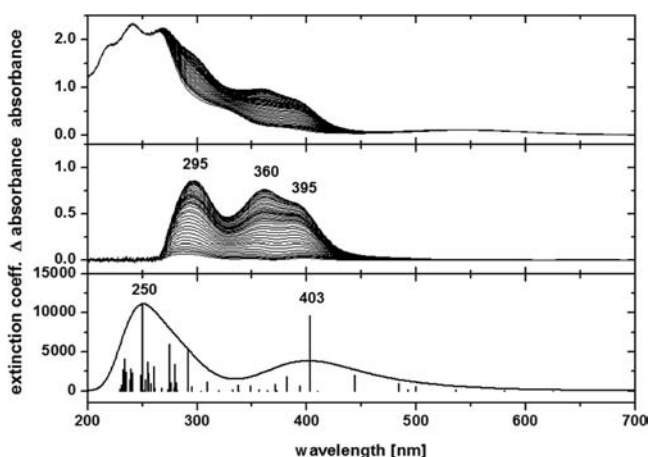


Figure 14. Comparison of the UV-vis spectra observed during electrochemical reduction of 2-MeCN in acetonitrile (top) and the calculated spectrum of $\tilde{5}$ (bottom, peak spectrum is multiplied with 10 for a better overview). Middle: Experimental difference spectra.

3. Mo(III) Ethylamido Complex 5H. To test whether reduction of 2-MeCN in the presence of acid leads to the observed suppression of the near-UV absorption features associated with the Mo(III) alkylidene intermediate, DFT calculations on the corresponding protonated species were performed as well. Geometry optimization of the Mo(III) ethylamido model complex $[\text{Mo}(\text{MeCN})(\text{HNEt})(\text{PH}_2\text{CH}_2\text{CH}_2\text{PH}_2)_2]^{2+}$ ($\tilde{5}\text{H}$) gives the structure shown in Figure 11, right. In this complex, the Mo–N–C angle is 134.8° and so even further decreased compared to the unprotonated species (154.8°), whereas the Mo–N(amido) distance increases to 1.92 \AA ($\tilde{5}$ 1.82 \AA , $\tilde{2}$ -MeCN 1.74 \AA). The Mo–N(acetonitrile) bond length, however, does not change with respect to $\tilde{5}$ (2.32 \AA ; cf. $\tilde{2}$ -MeCN 2.38 \AA). The MO scheme and designations of the molecular orbitals are given in the Supporting Information. Importantly, the SOMO of $\tilde{5}$ is greatly lowered in energy in $\tilde{5}\text{H}$, getting much more metal character. Correspondingly, Mulliken spin densities show a metal-centered radical (Mo 1.13 , N(NEt) -0.12), and the spin densities at the P atoms are five times larger as compared to $\tilde{5}$ (P(mean) 0.02 vs $\tilde{5}$ 0.004).

The calculated UV-vis spectrum of $\tilde{5}\text{H}$ is shown in Figure 16 and plotted in comparison to the experimental spectra

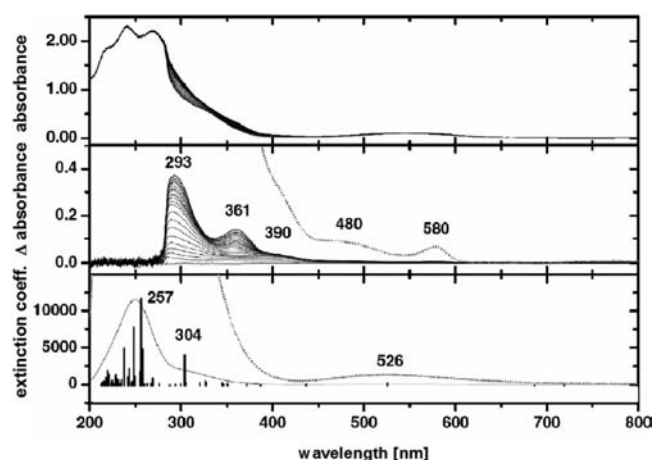


Figure 16. Comparison of the UV-vis spectra obtained during reduction of 2-MeCN in acetonitrile (top) and the calculated spectrum of $\tilde{5}\text{H}$ (bottom). (Middle) Experimental difference spectra. Spectra multiplied by 10 are drawn in dotted lines.

obtained during electrochemical reduction of 2-MeCN in the presence of phenol. Important transitions obtained by TDDFT are collected in Table 6. Besides a barely visible transition at 719 nm ($d_{xy} \rightarrow d_{yz_p_y}(\text{NEt})$) and a ligand-field transition of the single electron ($d_{xz} \rightarrow d_{yz_p_y}(\text{NEt})$) with no intensity, a transition at 526 nm is calculated, which corresponds to the charge-transfer transition ($p_y(\text{NEt})_d_{yz_p}(\text{P}) \rightarrow d_{yz_p_y}(\text{NEt})$). The intensity of this transition is, however, very low. In the near-UV region of the calculated spectrum there are some weak ligand-field transitions ($d_{xz} \rightarrow d_{x^2-y^2_p}(\text{P})$, $d_{xy} \rightarrow d_{x^2-y^2_p}(\text{P})$ and $d_{xy} \rightarrow d_{z^2_p}(\text{P})$). The first intense band at 304 nm corresponds to the $p(\text{P})_p(\text{NEt}) \rightarrow d_{yz_p_y}(\text{NEt})$ LMCT transition. Further intense bands are predicted at $\sim 260 \text{ nm}$, which are due to metal–ligand charge-transfer (MLCT) transitions, in particular, $d_{xz} \rightarrow p_y(\text{MeCN})$. The latter transition corresponds to the intense MLCT transition of $\tilde{5}$, which was located in the near-UV region in the experimental spectrum (vide supra).

To conclude, the theoretical spectrum associated with the Mo(III) ethylamido complex $\tilde{5}\text{H}$ confirms suppression of the near-UV absorption features associated with the unprotonated complex $\tilde{5}$, i.e., the metal \rightarrow acetonitrile MLCT transition

Table 5. Electronic Transitions of $\tilde{5}$ Obtained by TDDFT Calculations up to 300 nm

no.	energy/nm	oscillator strength	transition	type of transition
1	1872	0.0000	$d_{xz_p_x}(\text{NEt})\langle 80\text{A} \rangle \rightarrow d_{yz_p_y}(\text{NEt})\langle 81\text{A} \rangle$	
2	626	0.0000	$d_{xy}\langle 79\text{A} \rangle \rightarrow d_{yz_p_y}(\text{NEt})\langle 81\text{A} \rangle$	
3	581	0.0006	$d_{xy}\langle 79\text{B} \rangle \rightarrow d_{xz_p_x}(\text{NEt})\langle 80\text{B} \rangle$	LF
4	537	0.0008	$d_{xz_p_x}(\text{NEt})\langle 80\text{A} \rangle \rightarrow d_{x^2-y^2_p}(\text{P})\langle 85\text{A} \rangle$, $d_{xy}\langle 79\text{B} \rangle \rightarrow d_{yz_p_y}(\text{NEt})\langle 81\text{B} \rangle$	LF
5	500	0.0035	$p_y(\text{NEt})_d_{yz}\langle 78\text{A} \rangle \rightarrow d_{yz_p_y}(\text{NEt})\langle 81\text{A} \rangle$, $p_y(\text{NEt})_d_{yz}\langle 77\text{B} \rangle \rightarrow d_{yz_p_y}(\text{NEt})\langle 81\text{B} \rangle$	LMCT NeT \rightarrow Mo
6	493	0.0013	$d_{xz_p_x}(\text{NEt})\langle 80\text{A} \rangle \rightarrow d_{x^2-y^2_p}(\text{P})\langle 85\text{A} \rangle$	LF
7	485	0.0067	$d_{xz_p_x}(\text{NEt})\langle 80\text{A} \rangle \rightarrow p(\text{P})_p(\text{Mo})\langle 83\text{A} \rangle$	MLCT Mo \rightarrow P
8	444	0.0133	$d_{xz_p_x}(\text{NEt})\langle 80\text{A} \rangle \rightarrow p(\text{Mo})_p(\text{NCMe})\langle 82\text{A} \rangle$	
10	403	0.0644	$d_{xz_p_x}(\text{NEt})\langle 80\text{A} \rangle \rightarrow p_x(\text{NCMe})_p(\text{Mo})\langle 84\text{A} \rangle$	MLCT Mo \rightarrow NCMe
11	394	0.0041	$p_x(\text{NEt})_d_{xz}\langle 78\text{B} \rangle \rightarrow d_{yz_p_y}(\text{NEt})\langle 81\text{B} \rangle$	LMCT NeT \rightarrow Mo
12	382	0.0125	$p_x(\text{NEt})_d_{xz}\langle 78\text{B} \rangle \rightarrow d_{xz_p_x}(\text{NEt})\langle 80\text{B} \rangle$	LMCT NeT \rightarrow Mo
14	372	0.0055	$d_{xz_p_x}(\text{NEt})\langle 80\text{A} \rangle \rightarrow p(\text{Mo})_p_y(\text{NCMe})\langle 87\text{A} \rangle$	
17	349	0.0046	$d_{xz_p_x}(\text{NEt})\langle 80\text{A} \rangle \rightarrow p(\text{P})_p(\text{Mo})_s(\text{Mo})\langle 89\text{A} \rangle$	MLCT Mo \rightarrow P
19	338	0.0048	$d_{xz_p_x}(\text{NEt})\langle 80\text{A} \rangle \rightarrow p(\text{P})_s(\text{Mo})\langle 90\text{A} \rangle$	MLCT Mo \rightarrow P
22	309	0.0077	$d_{xy}\langle 79\text{A} \rangle \rightarrow p(\text{P})_p(\text{Mo})\langle 83\text{A} \rangle$	MLCT Mo \rightarrow P

Table 6. Electronic Transition in $\tilde{5}\text{H}$ from TDDFT Calculations

no.	energy/ nm	oscillator strength	transition	type of transition
3	719	0.0001	$d_{xy}(80\text{A}) \rightarrow d_{yz-p_y}(\text{NHet})(81\text{A})$	LF
4	686	0.0000	$d_{xz}(79\text{A}) \rightarrow d_{yz-p_y}(\text{NHet})(81\text{A})$	LF
5	526	0.0016	$p_y(\text{NHet})(78\text{A}) \rightarrow d_{yz-p_y}(\text{NHet})(81\text{A})$	LMCT
6	437	0.0001	$p(\text{P})_{-p_x}(\text{NHet})(78\text{B}) \rightarrow d_{xz}(79\text{B})$	LMCT
8	372	0.0001	$p(\text{P})_{-p}(\text{NHet})(77\text{B}) \rightarrow d_{xz}(79\text{B})$	LMCT
9	350	0.0011	$p(\text{P})(76\text{B}) \rightarrow d_{xz}(79\text{B}), d_{xy}(79\text{A}) \rightarrow d_{x^2-y^2-p}(\text{P})(82\text{A})$	LMCT
10	346	0.0006	$d_{xz}(79\text{A}) \rightarrow d_{x^2-y^2-p}(\text{P})(82\text{A})$	LF
11	345	0.0016	$p(\text{P})(76\text{B}) \rightarrow d_{xz}(79\text{B}), d_{xy}(79\text{B}) \rightarrow d_{x^2-p}(\text{P})(83\text{B})$	LMCT
12	327	0.0036	$d_{xy}(80\text{A}) \rightarrow d_{x^2-y^2-p}(\text{P})(82\text{A})$	LF
13	320	0.0024	$p(\text{P})_{-p}(\text{NHet})(77\text{A}) \rightarrow d_{yz-p_y}(\text{NHet})(81\text{A})$	LMCT
14	305	0.0014	$d_{xy}(80\text{A}) \rightarrow d_{x^2-p}(\text{P})(83\text{A})$	LF
15	304	0.0332	$p(\text{P})_{-p}(\text{NHet})(78\text{B}) \rightarrow d_{yz-p_y}(\text{NHet})(81\text{B})$	LMCT
24	258	0.0402	$d_{xz}(79\text{A}) \rightarrow p_y(\text{MeCN})(84\text{A}), p(\text{P})_{-d_{xy}}(75\text{B}) \rightarrow d_{yz-p_y}(\text{NHet})(81\text{B})$	MLCT
25	257	0.0970	$d_{xz}(79\text{A}) \rightarrow p_x(\text{MeCN})(85\text{A}), p(\text{P})_{-p}(\text{NHet})(77\text{B}) \rightarrow d_{yz-p_y}(\text{NHet})(81\text{B})$	MLCT

giving rise to this absorption is now shifted into the UV. This results from the fact that the singly occupied $d_{xz-p_x}(\text{Net})$ orbital (SOMO) of **5** is greatly stabilized due to protonation of the nitrogen atom of the alkylnitrene ligand, evolving into a d_{xz} orbital of dominant metal character in **5H**. As a consequence of the change in character of this orbital, the spin density is drastically decreased at the N atom of the NEt ligand and increased at the P atoms. The only intense transitions of **5H** in the UV–vis are calculated at 304 and 256 nm, so the region around 400 nm is predicted to be more or less transparent.

4. Mo(III) Ethylamido Complex 5H-OPh. As described above, reduction of 2-MeCN and 2-OTf in the presence of phenol initially leads to the Mo(III) ethylamido complex 5H-OPh (cf. Scheme 6), which is further reduced to the Mo(II) complex 7-OPh. The structure of 5H-OPh derived from geometry optimization is given in Figure 11, left. The corresponding MO schemes and TDDFT results are given in the Supporting Information. Due to the π -antibonding effect of the phenolate ligand, the singly occupied d_{xz} orbital is shifted to higher energy as compared to **5H**. The calculated spin densities at the phosphorus atoms of 5H-OPh, on the other hand, are not significantly increased with respect to **5H**. A possible reason may be the small magnitude of the calculated spin densities, rendering the correlation with observed coupling constants difficult. Importantly, the calculation predicts an intense phenolate \rightarrow Mo(III) LMCT transition at 580 nm. This transition is absent in the corresponding Mo(II) complex 7-OPh (see below). We therefore conclude from UV–vis spectroelectrochemistry, where no CT band is observed in this region (Figure 9), that reduction of 2-MeCN in the presence of phenol in fact leads to the Mo(II) complex 7-OPh, in agreement with the CV data.

5. Mo(II) Azavinylidene Complex 6 and Mo(II) Ethylamido Complexes 7 and 7-OPh. In order to assign the absorption spectra obtained in the UV–vis spectroelectrochemical experiments, it is necessary to further determine the electronic structures and UV–vis spectroscopic properties of the Mo(II) azavinylidene complex **6** and the Mo(II) ethylamido complexes

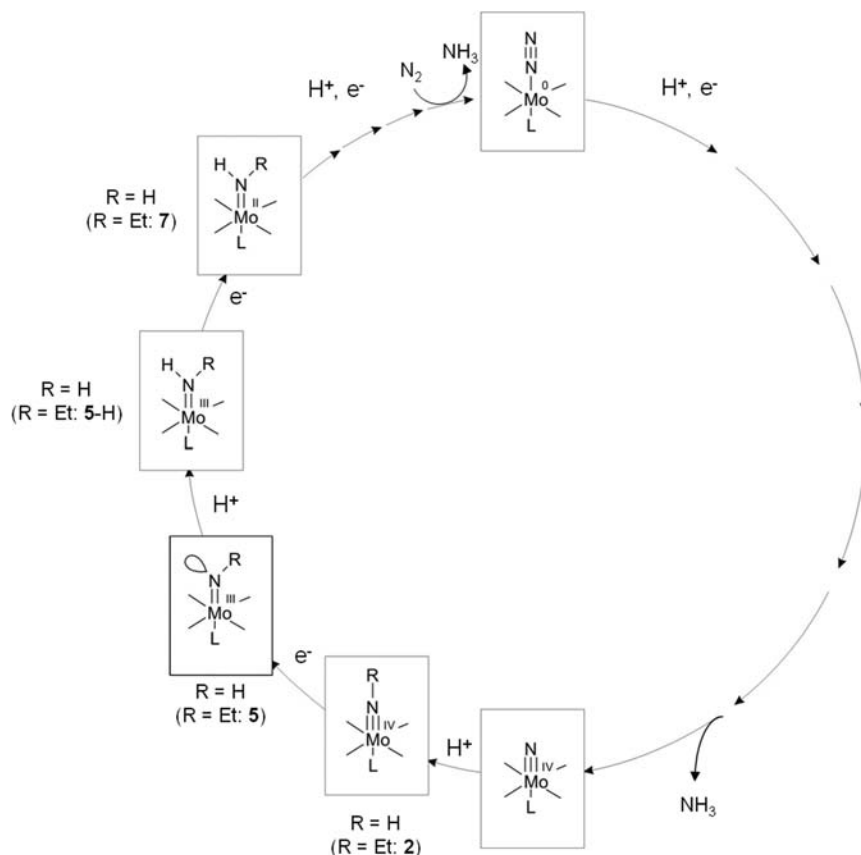
7 and **7-OPh** (cf. Schemes 4 and 6). Geometry-optimized structures of these complexes are shown in Figure 11. The corresponding MO schemes and TDDFT results are given in the Supporting Information. Importantly, the Mo(II) ethylamido complex **7** exhibits a structure that is very similar to that of the Mo(III) ethylamido complex **5H**, the additional electron residing in the d_{xz} orbital. TDDFT calculation indicates that this species (just as the Mo(III) ethylamido complex **5H**) shows no significant absorption in the near-UV region and thus cannot account for the intense absorption bands detected in the UV–vis spectroelectrochemical experiment above. The Mo(II) azavinylidene complex **6**, in contrast, does exhibit two bands in this region, i.e., at 356 and 332 nm (Supporting Information, Figure S24 and Table S8). The 356 nm band (which has a comparable oscillator strength to the 400 nm band predicted for **5**) may account for the second band detected at 360 nm in the UV–vis spectrum obtained upon reduction of 2-MeCN in the absence of phenol (Figure 14). As the lower energy band has been attributed to the Mo(II) alkylnitrene complex **5** the absorption spectrum obtained after reduction of 2-MeCN in acetonitrile thus may in fact be due to a mixture of **5** and **6**, as already inferred from the time dependence of the growth and disappearance of these bands (vide supra).

DFT and TDDFT calculations performed for complex 7-OPh are presented in the Supporting Information as well. In analogy to the Mo(II) and Mo(III) ethylamido complexes 5H-OPh and **7**, 7-OPh does not exhibit intense bands in the near-UV region. Furthermore, the intense phenolate \rightarrow Mo(III) CT transition, which has been predicted to be at 580 nm for 5H-OPh (vide supra), now is absent as the target orbital is doubly occupied in the Mo(II) d^4 configuration.

IV. SUMMARY AND CONCLUSION

In the preceding sections electrochemical and spectroelectrochemical investigations have been performed on Mo(IV) ethylimido complexes coordinated by depe coligands. Exchange of the trans ligand of the ethylimido–acetonitrile complex $[\text{Mo}(\text{MeCN})(\text{Net})(\text{depe})](\text{OTf})_2$ (2-MeCN) to yield the so far unknown complex $[\text{Mo}(\text{OTf})(\text{Net})(\text{depe})_2](\text{OTf})$ (2-OTf) could be proven by NMR and UV–vis spectroscopy as well as single-crystal X-ray diffractometry. Complex 2-MeCN has in turn been prepared from the NNH_2 complex $[\text{Mo}(\text{OTf})(\text{NNH}_2)(\text{depe})_2]\text{OTf}$ (1-OTf) by an already published route.¹⁵

2-MeCN and 2-OTf were subjected to cyclic voltammetric studies in solvents MeCN and THF and in the presence and absence of phenol. In order to obtain direct information on the corresponding electronic structure changes, the intermediates being formed during electrochemical reductions of 2-MeCN and 2-OTf were further investigated by UV–vis and EPR spectroelectrochemistry coupled to DFT calculations. Importantly, EPR data allowed us to detect two different Mo(III) species which were assigned to the complexes $[\text{Mo}(\text{HNet})(\text{depe})_2(\text{MeCN})]^{2+}$ (**5H**) and $[\text{Mo}(\text{HNet})(\text{depe})_2(\text{OPh})]^+$ (**5H-OPh**), respectively. UV–vis spectroelectrochemistry of 2-MeCN in the absence of phenol indicated formation of two intense CT bands in the near-UV region which were suppressed when phenol was present. TDDFT calculations allowed us to assign these bands to metal $\rightarrow \pi^*(\text{MeCN})$ LMCT transitions of Mo(III) and Mo(II) species containing acetonitrile ligands (see below) and, in agreement with the experimental observation, predicted the absence of these bands

Scheme 7. Overview of the Complexes Mentioned in This Study and Their Position in the Second Half of the Chatt Cycle^a

^aFor clarity, the equatorial phosphine donors have been omitted. Complex designations refer to $\text{L} = \text{CH}_3\text{CN}$.

in the reduction experiments where phenol had been added as an external proton source.

In the course of the CV investigations of 2-MeCN, an unprecedented Mo(III) intermediate was detected which formed in acetonitrile in the absence of a proton source and was assigned to be the Mo(III) alkylnitrene complex $[\text{Mo}(\text{NEt})(\text{CH}_3\text{CN})(\text{depe})_2]\text{OTf}$ (**5**). The fact that **5** is unstable in the CV experiment was ascribed to its reaction with the parent Mo(IV)ethylimido complex, giving the Mo(III) ethylamido and Mo(II) azavinylidene complexes **5H** and **6**, respectively. From coulometric data indicating an overall one-electron reduction of 2-MeCN it was concluded that **5H** can receive a second electron at the applied potentials, leading to the Mo(II) ethylamido complex **7**. In a combined proton/electron transfer reaction this complex may finally react with the azavinylidene complex **6** to regenerate the Mo(III) ethylimido complex **5**. As inferred from DFT, this species exhibits a bent Mo–N–C unit ($\sim 155^\circ$) and a Mo–N distance that is slightly elongated ($\sim 0.1 \text{ \AA}$) with respect to the Mo–N bond length of the parent Mo(IV) alkylnitrene complex **2**. The unpaired electron of **5** resides in a π orbital of mixed metal/NEt ligand character. A characteristic UV–vis spectroscopic signature of **5** is an intense MLCT transition from this SOMO into the π^* orbitals of the trans ligand (acetonitrile) at $\sim 400 \text{ nm}$. Importantly, no such transition in the near-UV region is predicted for both Mo(III) and Mo(II) alkylamido species, i.e., complexes **5H**, **5H-OPh**, **7**, and **7-OPh**. The only other species exhibiting an intense band in the UV is the azavinylidene complex **6** where this band, however, is predicted at somewhat higher energy ($\sim 350 \text{ nm}$). This suggests that the experimental spectrum obtained after

reduction of 2-MeCN in MeCN, which exhibits two bands at 395 and 360 nm, corresponds to a mixture of **5** and **6**.

EPR spectroelectrochemistry of the reduction of 2-MeCN in acetonitrile yields a quintet signal at $g \cong 2$. Due to the absence of significant nitrogen hyperfine couplings, however, this signal is not assigned to the unprotonated alkylnitrene complex **5** but to its protonated counterpart, the Mo(III) ethylamido complex **5H**. According to DFT, the Mo–C–N angle is reduced to 135° in this complex and the Mo–N bond length increased to 1.92 Å. The singly occupied, mixed metal–imide π orbital of **5** is greatly lowered in energy, leading to a primarily metal-type $d\pi$ (d_{xz} or d_{yz}) orbital with antibonding contributions of the axial ligands in **5H**. Single occupancy of this orbital along with double occupancy of the metal d_{xy} orbital correspond to a Mo(III) $S = 1/2$ low-spin configuration, as also found in the unprotonated alkylnitrene complex **5**. In **5H** the near-UV MLCT transition characteristic of **5** is shifted into the UV and the EPR spectrum exhibits a Mo–P hyperfine coupling constant of 18.34 G that is markedly increased with respect to **5** but still smaller than that found in Mo(V) imido complexes ($\sim 20 \text{ G}$). The LUMO of **5H** is the β -spin counterpart of the singly occupied, α -spin metal $d\pi$ orbital (d_{xz} or d_{yz}). Importantly, a Mo(III) ethylimido complex is also formed if an externally added proton source is present. In the case of phenol this leads to the Mo(III) alkylamido complex **5H-OPh** which exhibits a 50% larger ^{31}P hyperfine splitting constant as compared to **5H**.

One-electron transfer into the LUMOs of the Mo(III) alkylamido complexes **5H** or **5H-OPh** generates the Mo(II) alkylamido complexes **7** or **7-OPh**, which constitutes the next

step of the Chatt cycle. In agreement with the findings of Alias et al.,¹³ combined evidence of this paper indicates that an initial one-electron reduction is needed first for the Mo(IV) ethylimido complexes **2** to create a sufficiently basic Mo(III) alkynitrene species to add a proton. Then a second electron can be transferred at the same potential, forming a Mo(II) amido complex. This sequence of elementary steps represents remarkable support for the fundamental reaction mechanism of the Schrock and Chatt cycles, which dictates that double reductions (and double protonations) lead to high-energy intermediates and every reduction has to be followed by a protonation (and vice versa) to establish a minimum-energy pathway for dinitrogen reduction.

In Scheme 7 the complexes investigated in this study are integrated in the second part of the Chatt cycle. The first part of the Chatt cycle involves protonation and reduction of coordinated dinitrogen under formation of 1 equiv of ammonia and the nitrido complex. Note that also dinitrogen complexes with acetonitrile coligands (Scheme 6, top) exist that can be protonated under retention of the trans ligation.²⁹ Moreover, Mo(IV) nitrido and imido complexes with nitrile coligands exist.³⁰ From this perspective, molybdenum tetrphosphine complexes with acetonitrile coligands are in principle “ideal candidates” for N₂ fixing reactions following the Chatt cycle. In practice, however, these neutral trans ligands are displaced by the conjugate bases of the acids employed in the protonation reactions, as exemplified in the present study by the reductions of **2-MeCN** and **2-OTf** in the presence of phenol. For Mo phosphine systems having the potential to catalytically mediate conversion of N₂ to NH₃, these ligand-exchange reactions therefore have to be prevented by proper ligand design.⁸

■ ASSOCIATED CONTENT

■ Supporting Information

Additional NMR-, IR-, Raman, and EPR-spectra, as well as electrochemical data and details concerning the theoretical calculations. This material is available free of charge via the Internet at <http://pubs.acs.org>.

■ Related Articles

Reduction and Protonation of End-On-Coordinated Dinitrogen, Part VIII. Part VII: Dreher, A.; Mersmann, K.; Näther, C.; Ivanovic-Burmazovic, I.; van Eldik, R.; Tuzcek, F. *Inorg. Chem.* **2009**, *48* (5), 2078–2093.

■ AUTHOR INFORMATION

Corresponding Author

*E-mail: philipp.kurz@ac.uni-freiburg.de (P.K.); ftuzcek@ac.uni-kiel.de (F.T.).

Author Contributions

[§]The first two authors contributed equally to this work as main experimental investigators.

Notes

The authors declare no competing financial interest.

■ ACKNOWLEDGMENTS

Part of this work was funded by the Fonds der Chemischen Industrie (Liebig fellowship of P.K.). F.T. would like to thank the DFG and the Christian-Albrechts-University Kiel for generous support of this research.

■ REFERENCES

- (1) (a) MacKay, B. A.; Fryzuk, M. D. *Chem. Rev.* **2004**, *104*, 385–402. (b) Hinrichsen, S.; Broda, H.; Gradert, C.; Söncksen, L.; Tuzcek, F. *Annu. Rep. Prog. Chem., Sect. A: Inorg. Chem.* **2012**, *108*, 17–47.
- (2) Tuzcek, F. *Encyclopedia of Inorganic and Bioinorganic Chemistry*; John Wiley & Sons, Ltd.: New York, 2011.
- (3) Barney, B. M.; Lee, H.-I.; Dos Santos, P. C.; Hoffman, B. M.; Dean, D. R.; Seefeldt, L. C. *Dalton Trans.* **2006**, *35*, 2277–2284.
- (4) Hoffman, B. M.; Dean, D. R.; Seefeldt, L. C. *Acc. Chem. Res.* **2009**, *42*, 609–619.
- (5) Seefeldt, L. C.; Hoffman, B. M.; Dean, D. R. *Curr. Opin. Chem. Biol.* **2012**, *16*, 19–25.
- (6) Dreher, A.; Mersmann, K.; Näther, C.; Ivanovic-Burmazovic, I.; van Eldik, R.; Tuzcek, F. *Inorg. Chem.* **2009**, *48*, 2078–2093.
- (7) (a) Yandulov, D. V.; Schrock, R. R. *Science* **2003**, *301*, 76–78. (b) Arashiba, K.; Miyake, Y.; Nishibayashi, Y. *Nat. Chem.* **2011**, *3*, 120–125. (c) Nishibayashi, Y. *Nat. Chem.* **2011**, *3*, 502–504. (d) Hebden, T. J.; Schrock, R. R.; Takase, M. K.; Müller, P. *Chem. Commun.* **2012**, *48*, 1851–1853. (e) Schrock, R. R. *Nat. Chem.* **2011**, *3*, 95–96. (f) Munisamy, T.; Schrock, R. R. *Dalton Trans.* **2012**, *41*, 130–137. (g) Rodriguez, M. M.; Bill, E.; Brennessel, W. W.; Holland, P. L. *Science* **2011**, *334*, 780–783. (h) Lee, Y.; Mankad, N. P.; Peters, J. C. *Nat. Chem.* **2010**, *2*, 558–565.
- (8) Broda, H.; Hinrichsen, S.; Tuzcek, F. *Coord. Chem. Rev.* **2013**, *257*, 587–598.
- (9) (a) Tuzcek, F.; Horn, K. H.; Lehnert, N. *Coord. Chem. Rev.* **2003**, *245*, 107–120. (b) Pickett, C. J. *J. Biol. Inorg. Chem.* **1996**, *1*, 601–606.
- (10) (a) Lehnert, N.; Tuzcek, F. *Inorg. Chem.* **1999**, *38*, 1659–1670. (b) Lehnert, N.; Tuzcek, F. *Inorg. Chem.* **1999**, *38*, 1671–1682.
- (11) (a) Horn, K. H.; Lehnert, N.; Tuzcek, F. *Inorg. Chem.* **2003**, *42*, 1076–1086. (b) Horn, K. H.; Böres, N.; Lehnert, N.; Mersmann, K.; Näther, C.; Peters, G.; Tuzcek, F. *Inorg. Chem.* **2005**, *44*, 3016–3030. (c) Mersmann, K.; Horn, K. H.; Böres, N.; Lehnert, N.; Studt, F.; Paulat, F.; Peters, G.; Ivanovic-Burmazovic, I.; van Eldik, R.; Tuzcek, F. *Inorg. Chem.* **2005**, *44*, 3031–3045. (d) Tuzcek, F. In *Computational Inorganic and Bioinorganic Chemistry*. Solomon, E. I., Ed.; John Wiley & Sons Inc.: New York, 2009.
- (12) Henderson, R. A.; Leigh, G. J.; Pickett, C. J. *J. Chem. Soc., Dalton Trans.* **1989**, *18*, 425–430.
- (13) Alias, Y.; Ibrahim, S. K.; Queiros, M. A.; Fonseca, A.; Talarmin, J.; Volant, F.; Pickett, C. J. *J. Chem. Soc., Dalton Trans.* **1997**, *26*, 4807–4816.
- (14) (a) George, T. A.; Busby, D. C.; Iske, S. D. A., Jr. Photochemistry of Bis(dinitrogen)bis[1,2-bis(diphenylphosphino)ethane]molybdenum. In *Inorganic and Organometallic Photochemistry*; Wrighton, S. M., Ed.; American Chemical Society: Washington, DC, 1978; Vol. 168, Chapter 9, pp 147–157. (b) Bossard, G. E.; Busby, D. C.; Chang, M.; George, T. A.; Iske, S. D. A., Jr. *J. Am. Chem. Soc.* **1980**, *102*, 1001–1008.
- (15) Sivasankar, C.; Böres, N.; Peters, G.; Habeck, C. M.; Studt, F.; Tuzcek, F. *Organometallics* **2005**, *24*, 5393–5406.
- (16) Sheldrick, G. M. *Acta Crystallogr., Sect. A* **2008**, *64*, 112–122.
- (17) Becke, A. D. *J. Chem. Phys.* **1993**, *98*, 5648–5652.
- (18) Dunning, T. H. Jr.; Hay, P. J. In *Modern Theoretical Chemistry*; Schaefer, H. F., III, Ed.; Plenum: New York, 1976.
- (19) Frisch, M. J.; Trucks, G. W.; Schlegel, H. B.; Scuseria, G. E.; Robb, M. A.; Cheeseman, J. R.; Scalmani, G.; Barone, V.; Mennucci, B.; Petersson, G. A.; Nakatsuji, H.; Caricato, M.; Li, X.; Hratchian, H. P.; Izmaylov, A. F.; Bloino, J.; Zheng, G.; Sonnenberg, J. L.; Hada, M.; Ehara, M.; Toyota, K.; Fukuda, R.; Hasegawa, J.; Ishida, M.; Nakajima, T.; Honda, Y.; Kitao, O.; Nakai, H.; Vreven, T.; Montgomery, J. J. A.; Peralta, J. E.; Ogliaro, F.; Bearpark, M.; Heyd, J. J.; Brothers, E.; Kudin, K. N.; Staroverov, V. N.; Kobayashi, R.; Normand, J.; Raghavachari, K.; Rendell, A.; Burant, J. C.; Iyengar, S. S.; Tomasi, J.; Cossi, M.; Rega, N.; Millam, J. M.; Klene, M.; Knox, J. E.; Cross, J. B.; Bakken, V.; Adamo, C.; Jaramillo, J.; Gomperts, R.; Stratmann, R. E.; Yazyev, O.; Austin, A. J.; Cammi, R.; Pomelli, C.; Ochterski, J. W.; Martin, R. L.; Morokuma, K.; Zakrzewski, V. G.; Voth, G. A.; Salvador, P.; Dannenberg, J. J.; Dapprich, S.; Daniels, A. D.; Farkas, Ö;

Foresman, J. B.; Ortiz, J. V.; Cioslowski, J.; Fox, D. J. *Gaussian09*, Revision A.02; Gaussian Inc., Wallingford, CT, 2009.

(20) Kaim, W.; Ernst, S.; Kasack, V. *J. Am. Chem. Soc.* **1990**, *112*, 173–178.

(21) Stoll, S.; Schweiger, A. *J. Magn. Reson.* **2006**, *178*, 42–55.

(22) (a) Fairhurst, S. A.; Hughes, D. L.; Ibrahim, S. K.; Abasq, M.-L.; Talarmin, J.; Queiros, M. A.; Fonseca, A.; Pickett, C. J. *J. Chem. Soc., Dalton Trans.* **1995**, *24*, 1973–1984. (b) Bevan, P. C.; Chatt, J.; Dilworth, J. R.; Henderson, R. A.; Leigh, G. J. *J. Chem. Soc., Dalton Trans.* **1982**, *11*, 821–824. (c) Hughes, D. L.; Mohammed, M. Y.; Pickett, C. J. *J. Chem. Soc., Dalton Trans.* **1990**, *19*, 2013–2019.

(23) Hughes, D. L.; Lowe, D. J.; Mohammed, M. Y.; Pickett, C. J.; Pinhal, N. M. *J. Chem. Soc., Dalton Trans.* **1990**, *19*, 2021–2027.

(24) (a) Seini, H.; Tanabe, Y.; Ishii, Y.; Hidai, M. *Inorg. Chim. Acta* **1998**, *280*, 163–171. (b) Tanabe, Y.; Seini, H.; Ishii, Y.; Hidai, M. *J. Am. Chem. Soc.* **2000**, *122*, 1690–1699.

(25) Hayashida, T.; Kondo, H.; Terasawa, J.-i.; Kirchner, K.; Sunada, Y.; Nagashima, H. *J. Organomet. Chem.* **2007**, *692*, 382–394.

(26) Mersmann, K.; Näther, C.; Tuczek, F. *Acta Crystallogr., Sect. E* **2007**, *63*, m1476.

(27) Sivasankar, C.; Tuczek, F. *J. Chem. Soc., Dalton Trans.* **2006**, *35*, 3396–3398.

(28) Studt, F.; Tuczek, F. *Angew. Chem., Int. Ed.* **2005**, *44*, 5639–5642.

(29) Habeck, C. M.; Lehnert, N.; Näther, C.; Tuczek, F. *Inorg. Chim. Acta* **2002**, *337C*, 11–31.

(30) Mersmann, K.; Hauser, A.; Lehnert, N.; Tuczek, F. *Inorg. Chem.* **2006**, *45*, 5044–5056.